A fast hybrid (3-D/1-D) model for thermal radiative transfer in cirrus via successive orders of scattering

Thomas Fauchez, Anthony Davis, Céline Cornet, Frédéric Szczap, Steven Platnick, Philippe Dubuisson, François Thieuleux

AGU PUBLICATIONS

JGR

Journal of Geophysical Research: Atmospheres

RESEARCH ARTICLE
10.1002/2016JD025607

Key Points:
- Three-dimensional heterogeneous pixels lead to larger direct emission but smaller scattering contribution than 1-D homogeneous pixels
- On average, for thermal infrared wavelengths, 99% of the total radiance is computed after the third scattering
- Three-dimensional radiances can be approximated using an efficient hybrid model combining 3-D direct emission and 1-D scatterings

Correspondence to:
T. Fauchez,
thomas.j.fauchez@nasa.gov

Citation:
Fauchez, T., A. B. Davis, C. Cornet, F. Szczap, S. Platnick, P. Dubuisson, and F. Thieuleux (2017), A fast hybrid (3-D/1-D) model for thermal radiative transfer in cirrus via successive orders of scattering, *J. Geophys. Res. Atmos.*, *122*, 344–366, doi:10.1002/2016JD025607.

Received 5 JUL 2016
Accepted 4 NOV 2016
Accepted article online 11 NV 2016
Published online 6 JAN 2017

A fast hybrid (3-D/1-D) model for thermal radiative transfer in cirrus via successive orders of scattering

Thomas Fauchez[1,2], Anthony B. Davis[3], Céline Cornet[4], Frédéric Szczap[5], Steven Platnick[2], Philippe Dubuisson[4], and François Thieuleux[4]

[1]Universities Space Research Association, Greenbelt, Maryland, USA, [2]Climate and Radiation Laboratory, NASA Goddard Space Flight Center, Greenbelt, Maryland, USA, [3]Jet Propulsion Laboratory, California Institute of Technology, Pasadena, California, USA, [4]Laboratoire d'Optique Atmosphérique, UMR 8518, Université Lille 1, Villeneuve d'Ascq, France, [5]Laboratoire de Météorologie Physique, UMR 6016, Université Blaise Pascal, Clermont-Ferrand, France

Abstract We investigate the impact of cirrus cloud heterogeneity on the direct emission by cloud or surface and on the scattering by ice particles in the thermal infrared (TIR). Realistic 3-D cirri are modeled with the 3DCLOUD code, and top-of-atmosphere radiances are simulated by the 3-D Monte Carlo radiative transfer (RT) algorithm 3DMCPOL for two (8.65 μm and 12.05 μm) channels of the Imaging Infrared Radiometer on CALIPSO. At nadir, comparisons of 1-D and 3-D RT show that 3-D radiances are larger than their 1-D counterparts for direct emission but smaller for scattered radiation. For our cirrus cases, 99% of the 3-D total radiance is computed by the third scattering order, which corresponds to 90% of the total computational effort, but larger optical thicknesses need more scattering orders. To radically accelerate the 3-D RT computations (using only few percent of 3-D RT time with a Monte Carlo code), even in the presence of large optical depths, we develop a hybrid model based on exact 3-D direct emission, the first scattering order from 1-D in each homogenized column, and an empirical adjustment linearly dependent on the optical thickness to account for higher scattering orders. Good agreement is found between the hybrid model and the exact 3-D radiances for two very different cirrus models without changing the empirical parameters. We anticipate that a future deterministic implementation of the hybrid model will be fast enough to process multiangle thermal imagery in a practical tomographic reconstruction of 3-D cirrus fields.

1. Introduction

Cirrus clouds cover on average between 15% and 40% of the Earth's surface [*Sassen et al.*, 2008]. They are relevant components of the Earth's climate and radiation budget, but their role is still poorly understood. The temperature difference between the cloud top and the surface leads to a warming of the atmosphere by capturing a part of the infrared radiation emitted by the Earth's surface. In contrast, a part of the solar incident radiation is reflected to space, but it is generally small for high clouds. Cirrus clouds tend to lead to a positive radiative forcing (e.g., a greenhouse effect) although this will depend on their optical thickness [*Jensen et al.*, 1994], altitude [*Corti and Peter*, 2009], temperature [*Katagiri et al.*, 2013], and ice crystal effective size [*Min et al.*, 2010]. *Baran and Francis* [2004] have shown that any changes to cirrus microphysical characteristics will have a substantial feedback on climate change.

Global satellite observations are well suited to better understand cloud evolution and characteristics: cloud coverage, altitude, water content, optical properties, radiative impact, and so on. Many satellite missions are thus dedicated to observations from visible to microwave spectral ranges. Satellite imager retrievals of cirrus cloud optical thickness and ice crystal effective particle size, such as those from the Moderate Resolution Imaging Spectroradiometer (MODIS) [*Nakajima and King*, 1990; *Platnick et al.*, 2003, 2015], use solar reflectance observations from a combination of a nonabsorbing or slightly absorbing visible channel and an absorbing channel in the near infrared (NIR) or in the shortwave infrared (SWIR) or midwave infrared (MWIR) ranges. Thermal infrared (TIR) retrieval techniques are also used for cirrus made of ice particles with small effective radii; examples are the split-window technique [*Inoue*, 1985] for the advanced very high resolution radiometer [*Parol et al.*, 1991] or the operational algorithm for the Imaging Infrared Radiometer (IIR) on the CALIPSO satellite [*Garnier et al.*, 2012, 2013] or optimal estimation methods [*Rodgers*, 2000] for the Atmospheric Infrared Sounder V6 (AIRS) [*Kahn et al.*, 2014, 2015] and for MODIS [*Wang et al.*, 2014, 2016a, 2016b].

The main advantage of the optimal estimation method is that it allows a combination of different wavelength ranges, generally from visible to thermal infrared ranges to retrieve the cloud properties [*Cooper et al.*, 2007; *Sourdeval et al.*, 2015].

For both solar and IR retrievals, current global operational algorithms assume that the observational pixels are homogeneous and independent of their neighbors, i.e., the independent pixel approximation (IPA) [*Cahalan et al.*, 1994]. Each pixel content is considered horizontally infinite, leading to zero horizontal transport between them. However, in the real atmosphere, the radiative transfer (RT) occurs in all three spatial dimensions and clouds are neither horizontally nor vertically homogeneous. *Hogan and Kew* [2005] show, for cirrus clouds, that RT calculations using IPA can lead to errors on the mean top-of-atmosphere (TOA) radiative fluxes by about 45 W/m^2 in the shortwave and 15 W/m^2 in the longwave. Furthermore, *Chen and Liou* [2006] show that a significant impact exists on the broadband thermal cooling rates as well (around 10%). Concerning remote sensing applications, *Fauchez et al.* [2012, 2014] show that at the spatial resolution of polar-orbiting satellites (∼1 km), horizontal heterogeneity effects in the TIR spectrum are dominated by the "PPA" bias. This so-called plane-parallel approximation bias [*Cahalan et al.*, 1994] is due to the subpixel cloud homogeneity assumption. It occurs because of the nonlinearity of radiative quantities (reflectances, radiances, or brightness temperatures) with respect to the optical thickness. Indeed, 3-D radiative quantities computed for a three-dimensional (3-D) heterogeneous optical property field and then averaged at a given scale are different from one-dimensional (1-D) radiative quantities of averaged 3-D optical properties at the given scale.

Because cloud retrieval algorithms assume that the RT occurs in a 1-D medium, errors due to subpixel cloud inhomogeneities will obviously appear in the retrieved cloud products. PPA and IPA biases occur in the solar and TIR ranges alike, but their relative impact on the TOA radiative quantities is different in the two spectral ranges. Indeed, for solar reflectance channels, the IPA has a larger impact than in the TIR (the number of scattering orders and the mean paths are larger). This can lead to significant retrieval errors due to a larger horizontal transport of radiation between cloudy columns, as well as brightening and shadowing effects that are more difficult to quantify [*Várnai and Davies*, 1999; *Várnai and Marshak*, 2001; *Marshak and Davis*, 2005; *Oreopoulos and Cahalan*, 2005,]. In the TIR, absorption is stronger and leads to a large PPA bias but a smaller horizontal transport and thus a weaker IPA error [*Fauchez et al.*, 2014, 2015]. By comparing the AIRS V6 [*Kahn et al.*, 2014] and MODIS "Collection 6" retrievals [*Platnick et al.*, 2015], *Kahn et al.* [2015] showed that the sensitivity of cloud property retrieval to parameters such as the horizontal cloud heterogeneity, determination of the cloud top thermodynamic phase, and cloud vertical structure is strongly dependent on the observation wavelength. In addition, even for the most homogeneous scene that they identified (where AIRS and MODIS optical thickness are consistent), a difference of 5 to 10 μm remains between AIRS and MODIS effective radius retrievals, because of RT differences in the visible and infrared bands.

To better understand the effects of cloud heterogeneity on TOA thermal radiative quantities and potentially correct cloud parameter retrievals, 3-D RT simulations are essential. They allow us to model the impact of cloud heterogeneity on cloud scattering for given microphysical/optical properties, conditional that these properties are realistic. However, full 3-D RT calculations are generally very time consuming, particularly in Monte Carlo simulations. The aim of this paper is to better understand the contribution of the different orders of scattering in the TIR atmospheric window, as has already been done in the solar spectrum [*Chepfer et al.*, 1999; *Reichardt et al.*, 2000; *Wang et al.*, 2005; *Garnier et al.*, 2015]). Our present motivation is to propose a simplified 3-D RT model that has the advantage of being very fast compared to a full 3-D RT model.

In this work, we thus focus our attention on the contributions of successive orders of scattering inside a heterogeneous cirrus cloud, with different scattering properties, for two of the three IIR thermal infrared channels, at 8.65 μm (bandwidth 0.9 μm) and 12.05 μm (bandwidth 1.0 μm). In section 2, we present the different codes used in this study to generate 3-D realistic cirrus fields and to simulate the 3-D RT. In section 3, we study the differences between 3-D and 1-D RT in terms of contribution of the successive orders of cloud scattering to the total radiance observed at TOA. Section 4 presents a hybrid model based on exact 3-D direct emission and 1-D first scattering order in each homogenized column, followed by an empirical adjustment linearly dependent on the optical thickness to radically accelerate the 3-D RT computations. A summary and outlook are offered in section 5.

2. Cirrus Cloud and Radiative Transfer Models

2.1. Modeling Realistic 3-D Cirrus Fields

To model realistic 3-D cirrus fields, we use the 3DCLOUD code [*Szczap et al.*, 2014]. 3DCLOUD is a flexible 3-D cloud generator developed to simulate synthetic but realistic stratocumulus, cumulus, and cirrus cloud fields. 3DCLOUD simulations are faster than large eddy simulations. Several cloud properties pertinent to RT can be independently tuned by the user. To generate 3-D cirrus fields, 3DCLOUD solves, in a first step, drastically simplified Navier-Stokes/Boussinesq equations for atmospheric motion. In a second step, a Fourier filtering method is used to constrain scale invariant properties (spectral distribution of the optical thickness following a power law with a constant $-5/3$ exponent), the mean value, and the heterogeneity parameter of these 3-D cloud structures. The heterogeneity parameter of the optical thickness field is defined as $\rho_\tau = \mathrm{StDev}[\tau]/\bar{\tau}$ [*Szczap et al.*, 2000], where the numerator is the standard deviation of the optical thickness estimated from the pixel spatial resolution to the whole field and $\bar{\tau}$ is the mean value of the optical thickness across the whole field. Figure 1 shows the optical thickness at 12.05 μm (a) and IWC (b) of the cirrus (we will call it "cirrus 1") generated by 3DCLOUD and used in this study. To generate cirrus clouds, we used the standard midlatitude summer meteorological profile [see, e.g., *Fauchez et al.*, 2014; *Szczap et al.*, 2014; *Fauchez et al.*, 2015], and periodic boundary conditions were applied at the opposing edges of the domain. The surface is considered perfectly black (vanishing surface albedo) with a uniform temperature of 294.2 K.

The wave number energy spectrum of optical thickness in clouds, in general [*Cahalan and Snider*, 1989; *Davis et al.*, 1994, 1996, 1997; *Benassi et al.*, 2004, etc.], and cirrus clouds in particular [*Hogan and Kew*, 2005; *Fauchez et al.*, 2014; *Szczap et al.*, 2014] typically follow a power law with exponent $-5/3$ from an inner scale determined by complex turbulence-microphysics interactions [*Davis et al.*, 1999; *Gerber et al.*, 2001] to an outer scale where mesoscale effects (vertical wind shear, thermal stratification, and sedimentation processes) break the spectral slope one way or another. Although some studies [*Kew*, 2003; *Hogan and Kew*, 2005; *Wang and Sassen*, 2008] show that a scale break can appear roughly between 5 and 10 km for cirrus, we adopt a power law spectrum for the optical thickness with a constant exponent of $-5/3$. The eventual change of the sensitivity of this exponent due to mesoscale dynamical processes, and its implications for radiative transfer, will be the subject of a future work.

2.2. The Heterogeneous Cloud Optical Property Model

The aim of this work is to study the thermal infrared scattering through a cirrus cloud and more particularly the impact of the horizontal and vertical variabilities of the optical properties on the scattering. In order to represent RT through a 3-D heterogeneous cirrus optical property field the most accurately and as efficiently as possible, we use the *Baran* [2012] and *Baran et al.* [2013] optical property parameterization. *Baran et al.* [2009] have first shown that cirrus optical properties (extinction coefficient, single-scattering albedo, and asymmetry factor) could be related to the ice water content (IWC) and the temperature. This relation was obtained thanks to more than 20,000 particle size distributions measured during airborne campaigns [*Field et al.*, 2005, 2007]. Using the 3-D IWC and temperature fields simulated by the 3DCLOUD model, we thus convert these fields into realistic 3-D fields of extinction and absorption coefficients. For simplicity, we use the Henyey-Greenstein phase function with the asymmetry parameter of the parameterization to simulate the RT as used in the IIR retrieval algorithm [*Garnier et al.*, 2012, 2013]. In the TIR spectral region, this is a reasonable approximation of the phase function for most of the crystals [*Yang et al.*, 2001], conditional that the shape is not too irregular [*Baum et al.*, 2005a, 2005b]. Figure 2 shows optical property profiles averaged over the 10×10 km^2 cirrus field. We see that the extinction coefficient is similar at 8.65 μm and at 12.05 μm, but the single-scattering albedo and asymmetry factor are larger at 8.65 μm, leading to greater scattering contributions, particularly in the forward peak. The optical property field is then used as input of our 3-D RT code (see section 2.3) to simulate the RT through different viewing configurations (see section 3).

2.3. Radiative Transfer Simulations

In this study, we use the 3DMCPOL Monte Carlo code [*Cornet et al.*, 2010; *Fauchez et al.*, 2012, 2014]. This code is able to simulate the 3-D RT from the visible/near-IR (VNIR) range, including the state of polarization of the light, to the TIR. In this code, the atmosphere is divided into 3-D voxels with a constant horizontal size but a variable vertical size across the horizontal grid. Cyclic conditions are applied at the cloud field edges. Each voxel is defined by its optical properties given, for cirrus 1, by the *Baran* [2012] and *Baran et al.* [2013] parameterization that converts IWC and absolute temperature T into (i) extinction coefficient σ_e; (ii) single-scattering albedo $\varpi_0 = \sigma_s/\sigma_e$, the nondimensional ratio of scattering to extinction coefficients; and (iii) asymmetry factor

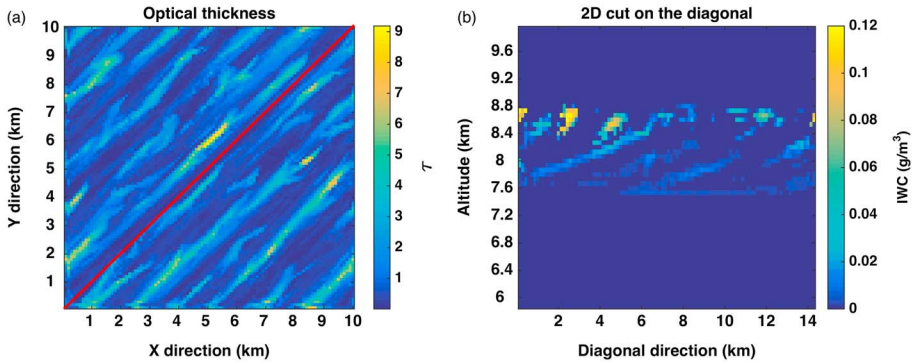

Figure 1. (a) Optical thickness (τ) at 12.05 μm of the 10×10 km^2 cirrus 1 field and (b) vertical distribution of IWC along the diagonal (red line) in Figure 1a. Mean optical thickness $\bar{\tau} = 1.2$, and the heterogeneity parameter of the optical thickness $\rho_\tau = 0.4$.

g of the nondimensionalized scattering phase function $P(\theta_s)$, where θ_s is the scattering angle. We used the Henyey-Greenstein model for $P(\theta_s)$ that is parameterized with g. Further on, we use an alternative parameterization.

Let $I(\boldsymbol{x}, \boldsymbol{\Omega})$ denote the five-dimensional (three spatial and two angular) radiance field at some fixed wavelength. Three-dimensional RT in the TIR is described in integral form by

$$I(\boldsymbol{x}, \boldsymbol{\Omega}) = \int_0^{\ell_{\max}} \left[\sigma_a(\boldsymbol{x}_\ell) B[T(\boldsymbol{x}_\ell)] + S(\boldsymbol{x}_\ell, \boldsymbol{\Omega})\right] \exp(-\tau(\boldsymbol{x}_\ell, \boldsymbol{x}))\mathrm{d}\ell + \left[\epsilon(\boldsymbol{x}_{\max}) B[T(\boldsymbol{x}_{\max})] + F_{\mathrm{dn}}(\boldsymbol{x}_{\max})\left[1 - \epsilon(\boldsymbol{x}_{\max})\right]\frac{\Omega_z}{\pi}\right] \exp(-\tau(\boldsymbol{x}_{\max}, \boldsymbol{x})), \quad (1)$$

where $\boldsymbol{x}_\ell = \boldsymbol{x} - \ell\boldsymbol{\Omega}$ is a point at distance ℓ from $\boldsymbol{x}$ along $-\boldsymbol{\Omega}$ (with $\boldsymbol{\Omega} = (0, 0, 1)^\mathrm{T}$ indicating zenith) and $\ell_{\max}$ is that distance to the boundary of the medium. $\tau(\boldsymbol{x}, \boldsymbol{x}')$ is optical distance, i.e., extinction $\sigma_e(\boldsymbol{x})$ integrated along a straight line from $\boldsymbol{x}$ to $\boldsymbol{x}'$. $\sigma_a(\boldsymbol{x})$ is the spatially varying absorption coefficient, while $B(T)$ is the Planck black-body radiance function that varies spatially according to absolute temperature $T(\boldsymbol{x})$. Their product is the volume source *term* for pure thermal emission.

As soon as the medium is not a perfect absorber (i.e., $\sigma_a < \sigma_e$), we need to account for one or more scatterings, which is done by adding the volume source *function*:

$$S(\boldsymbol{x}, \boldsymbol{\Omega}) = \frac{\sigma_s(\boldsymbol{x})}{4\pi} \int_{4\pi} P(\boldsymbol{x}, \cos^{-1}(\boldsymbol{\Omega}' \cdot \boldsymbol{\Omega}))I(\boldsymbol{x}, \boldsymbol{\Omega}')\mathrm{d}\boldsymbol{\Omega}', \quad (2)$$

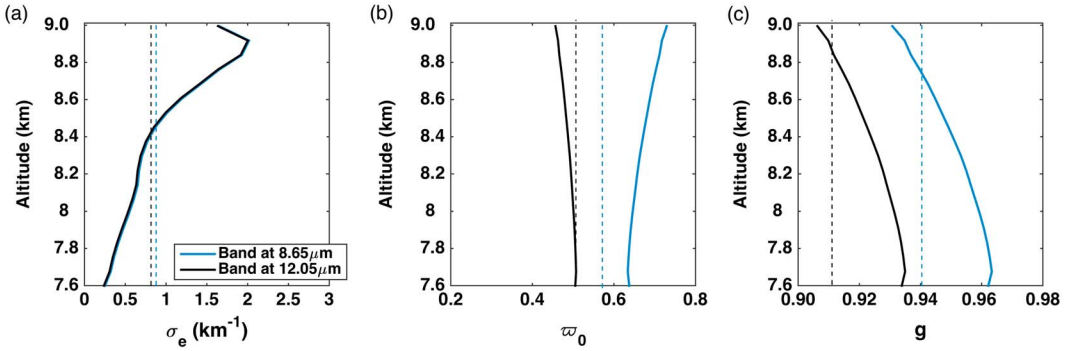

Figure 2. (a) Extinction coefficient σ_e in km^{-1}, (b) single-scattering albedo ϖ_0, and (c) asymmetry factor g as a function of the altitude for bands at 8.65 μm (thinner blue lines) and 12.05 μm (thicker black lines). Bold lines represent the vertical variation of the horizontally averaged optical property, and dashed lines correspond to the optical property obtained from vertically averaging the IWC. Note that the strong nonlinearities of the *Baran and Francis* [2004] parameterization make the latter nothing like the mean of the former.

where $\sigma_s(\boldsymbol{x}) = \sigma_e(\boldsymbol{x}) - \sigma_a(\boldsymbol{x})$ is the spatially varying scattering coefficient and $P(\boldsymbol{x}, \theta_s)$ is the spatially varying phase function.

The physical meaning of the line integral in (1) is an upwind "sweep" through the optical medium that collects and propagates the radiation sources from the sensor to the opposite boundary. In the present study, we are only interested in space-based instruments, so we have $\Omega_z > 0$. Also, we need to add the radiation that originates at the lower boundary, which is done in the second line of (1). Again, we have a pure thermal emission term, Planck's function for the boundary temperature times the local value of the surface emissivity, $\epsilon(\boldsymbol{x}_{\max}) = \epsilon(\boldsymbol{x}_{\ell_{\max}})$. Also, if that emissivity is not perfect ($\epsilon < 1$), then we need to add a term for one or more surface reflections, which is $1 - \epsilon$ (surface albedo) times Ω_z/π (surface phase function for Lambertian reflection) times the local value of downwelling irradiance:

$$F_{\mathrm{dn}}(\boldsymbol{x}_{\max}) = \int_{\Omega_z<0} |\Omega_z| I(\boldsymbol{x}_{\max}, \boldsymbol{\Omega}) \mathrm{d}\boldsymbol{\Omega}. \tag{3}$$

Together, (1)–(3) define mathematically the 3-D RT problem as a five-dimensional integral equation, as soon as the upper boundary condition is specified. Formally, that can be done using (1) for $\Omega_z < 0$ with $\epsilon(\boldsymbol{x}_{\max}) = 1$ (thus defeating the potential for a reflection) and $T(\boldsymbol{x}_{\max}) = 2.78$ K (although, in practice, it suffices to set $B[T(\boldsymbol{x}_{\max})] = 0$).

In the polarized RT framework used here, I is replaced by the Stokes vector $\mathbf{I} = [I, Q, U, V]$, and to describe the volume and surface interactions, the phase function $P(\cdot)$ and emissivity $\epsilon(\cdot)$ become 4×4 matrices [e.g., *Cornet et al.*, 2010]. For instance, a uniform depolarizing surface is represented by ϵ diag[1, 0, 0, 0]. Being the upper left-hand element of the phase matrix, the phase function is then denoted $P_{11}(\cdot)$. Current TIR satellite sensors, however, do not measure Stokes vector components beyond I.

To obtain purely emitted (not scattered nor reflected) radiation $I_0(\boldsymbol{x}, \boldsymbol{\Omega})$, we set $\sigma_s \equiv 0$, in (2), thus annulling the source function $S(\boldsymbol{x}, \boldsymbol{\Omega})$ in the first line of (1), along with $\epsilon \equiv 1$, thus defeating the surface reflection term in the second line of (1). We note that this is then a closed-form computation that can be performed deterministically (hence efficiently and accurately) for an arbitrary 3-D gridded field for $\sigma_e(\boldsymbol{x})$, $\varpi_0(\boldsymbol{x})$, $T(\boldsymbol{x})$, and $\epsilon(x, y, 0)$; see appendix. We also note that in many operational remote sensing retrieval schemes I_0 is used as an approximation for I in the TIR spectrum. We will see further on that this is not justifiable in the presence of cirrus clouds, neither in 1-D nor in 3-D.

The Monte Carlo (aka random quadrature) RTE solution method consists in successively iterating the substitution of (2)–(3) into (1), each time picking up one new order of scattering or reflection. We thus obtain $I_n(\boldsymbol{x}, \boldsymbol{\Omega})$ for $n \geq 0$ and, at least formally, we have

$$I(\boldsymbol{x}, \boldsymbol{\Omega}) = \sum_{n=0}^{\infty} I_n(\boldsymbol{x}, \boldsymbol{\Omega}), \tag{4}$$

the so-called Neumann series in the general theory of integral equations. Monte Carlo simulation of RT in the atmosphere, which is done technically by emitting and following Fictive Light Particles (FLIPs [*Pujol*, 2015]) using well-known random quadrature rules for propagation and scattering interactions with clouds or the surface. After a large number of FLIPs have been generated/followed, one averages detection or escape events over all the trajectories. In practice, the sum in (4) is truncated at a preset maximum or when small preset history "weight" threshold is crossed. These history termination criteria must be set so that the history almost always ends in escape from the medium.

For predicting TOA radiances, as observed by satellites, the 3DMCPOL code uses the Local Estimation Method (LEM) [*Marshak and Davis*, 2005; *Mayer*, 2009] that consists of computing the contribution of emission, scattering, or reflection events into the detector direction, attenuated by the medium optical thickness between the point of interaction and the detector in the prespecified direction [*Fauchez et al.*, 2014]. The medium optical thickness for gaseous absorption is parametrized with the correlated k-distribution [*Lacis and Oinas*, 1991; *Kratz*, 1995], and the equivalence theorem [*Partain et al.*, 2000; *Emde et al.*, 2011] is invoked. This consists of attaching an absorption vector $W_g(i_{\mathrm{bin}})$ to the estimate, with a magnitude determined by the number of bins "n_{bin}" of the adopted correlated k-distribution, with i_{bin} being the bin number ranging from 1 to n_{bin}. By cumulating separately each order of scattering, the LEM allows us to know the contribution of the

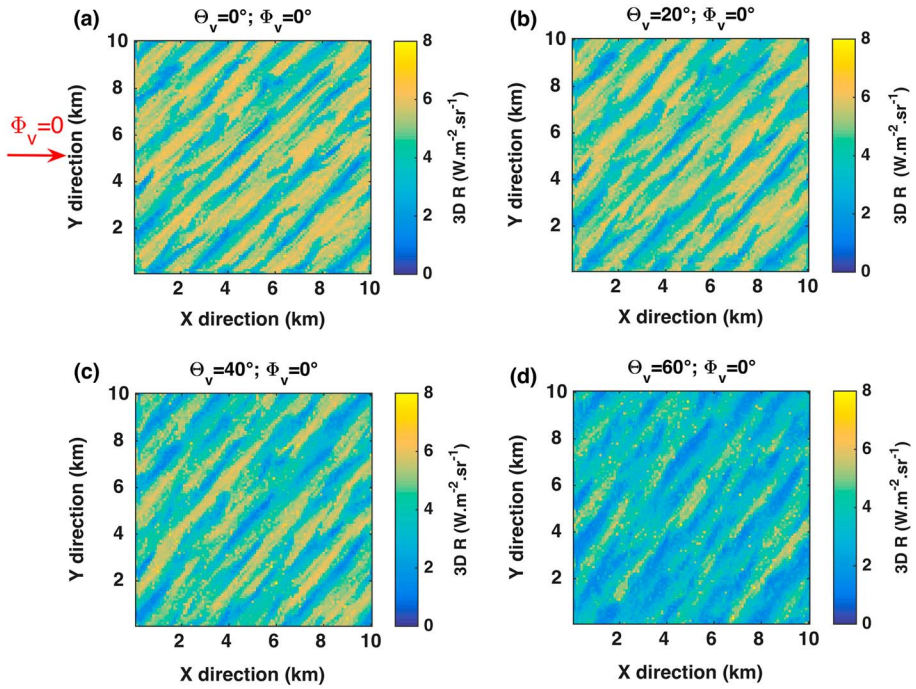

Figure 3. Three-dimensional radiance R (W m^{-2} sr^{-1}) fields of the cirrus in Figure 1 for various viewing zenith angles Θ_v: (a) 0°, (b) 20°, (c) 40°, and (d) 60° with azimuth view angle Φ_v set to 0, with indicator in Figure 3a. Wavelength is 8.65 μm, which has more particle scattering and gaseous opacity than the longer one.

emission order and each scattering order (s.o.) to the total radiance. The LEM weight at each s.o. as a function of bin number i_{bin} is calculated as

$$W_{le}(i_{bin}) = W_g(i_{bin})\, W_{\varpi_0} \frac{P_{11}(\theta_s)\exp(-\tau_{esc})}{4\pi\ \cos\Theta_v} \tag{5}$$

with W_{ϖ_0} being the weight due to the cloud extinction, initially equal to 1 and multiplied, at each cloud scattering, by the single-scattering albedo ϖ_0. We assumed that when W_{ϖ_0} is less than 10^{-8}, the contribution of the FLIP is negligible and a new one is launched. P_{11} is the first diagonal element of the nondimensionalized scattering matrix giving the probability of a FLIP to be scattered in the detector direction, θ_s is the angle between the FLIP direction and the detector, τ_{esc} is the optical distance in the medium from the interaction position to the space-based detector, and Θ_v is the viewing zenith angle. For a surface reflection, the same expression is used with its albedo $(= 1 - \epsilon)$ multiplying the weights and with its normalized bidirectional reflectivity distribution function ($1/\pi$ for the assumed Lambertian surface) replacing the phase function $P_{11}/4\pi$ and without dividing by $\cos\Theta_v$ since there is no thickness (hence air mass factor).

In Figure 3, we can see radiance fields simulated by 3DMCPOL and corresponding to the cirrus of Figure 1 in the band at 8.65 μm for four different viewing zenith angles ($\Theta_v = 0°$, 20°, 40°, and 60° with $\Phi_v = 0°$). The stripes are typical of uncinus cirrus, with the blue color corresponding to large optical thicknesses and yellow to small optical thicknesses. As Θ_v increases, radiance decreases by virtue of the increase of the mean geometrical path through the cloud from emission to detection.

3. Differences Between 3-D and 1-D Emission and Scattering Orders

Here we focus on the differences between 1-D and 3-D RT (separating the impacts of horizontal and vertical heterogeneities) as well as the influence of the vertical variability of optical properties for 1-D RT simulations. The calculations are done at 1 km spatial resolution, which is typical for sensors such as MODIS or IIR. For 1-D simulations, IWC and temperature profiles are horizontally averaged from 100 m to 1 km and then the optical property parameterization is used to estimate the optical coefficients. The IWC is also vertically averaged to test the impact of the vertical variability of optical properties on scattering. Three-dimensional simulations are

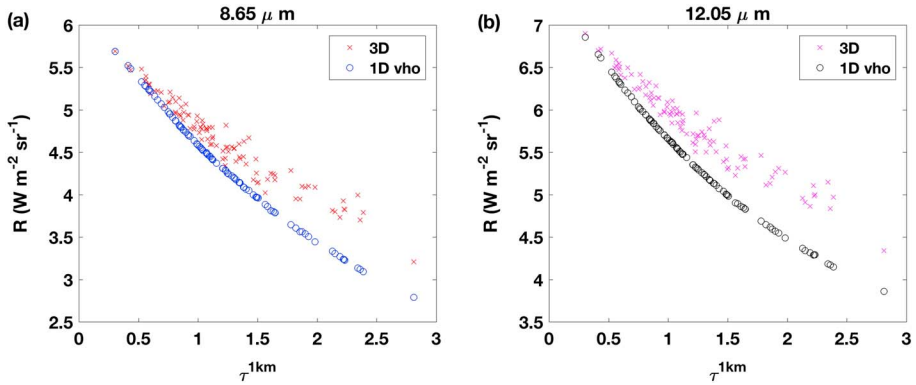

Figure 4. Radiances for 3-D (red crosses) and vertically homogeneous optical properties (1-D vho, blue circles) as a function of the optical thickness (τ^{1km}) for the bands at (a) 8.65 μm and (b) 12.05 μm.

performed at 100 m resolution with vertically heterogeneous cloud columns, and the radiances are then averaged to 1 km to compare with 1-D counterparts. Therefore, different cases are proposed (1) 3-D RT simulations with a 3-D heterogeneous (horizontally and vertically) optical property cloud field with the RT calculation first performed at 100 m and then the results averaged to 1 km and (2) 1-D RT simulations at 1 km with different vertical conditions:

1. One-dimensional "vho": vertically homogeneous optical properties. The IWC and temperature are vertically averaged in each cloudy column leading to a unique averaged value of σ_e, ϖ_0, and g.
2. One-dimensional "vhe": vertically heterogeneous optical properties. σ_e, ϖ_0, and g vary vertically.

Note that we do not perform 3-D computations at 1 km since this spatial resolution is much larger than the FLIP mean free path in the TIR (<500 m for a cirrus with an optical thickness of about unity; see *Fauchez et al.* [2014] for more details) leading to the fact that 1 km 3-D and 1-D computations are almost equivalent.

3.1. Differences Between 3-D and 1-D Scatterings for Nadir View

To introduce differences between 3-D and 1-D radiative transfer, we can see in Figure 4 3-D and 1-D vho TOA nadir radiances as a function of the 1 km optical thickness (denoted τ^{1km}) for the channel at 8.65 μm (a) and 12.05 μm (b). Three-dimensional radiances are larger than 1-D vho radiances due to the PPA and the difference increase with τ^{1km} as already shown by *Fauchez et al.* [2012, 2014].

In order to assess how the emission order (i.e., nonscattered radiation) or the scattering orders are responsible for these differences, we separate the radiance contribution of each order in Figure 5. It shows the thermal infrared radiances R (in W/m^2/sr) in 3-D, 1-D vho, and 1-D vhe as a function of τ^{1km} from the emission to the s.o. $n = 5$, with emission defined as $n = 0$, for the same cirrus cloud for the band at 8.65 μm.

The RT computations were done for a maximum s.o. limited to 10, which is by far enough for thermal infrared scattering. Indeed, at the tenth s.o., our simulations show that the contribution to the total radiance is of about 0.001 W/m^2/sr. In Figure 5, we only considered the first five s.o. as from the sixth order, the contribution to the total radiance under 0.5% at all the optical thicknesses. We can see that all the 1-D vho and 1-D vhe cases are very similar in terms of radiance, whatever the s.o., which means that the vertical variability of the optical properties is not very important in the 1-D computation of nadir radiances. We can, however, notice that the difference is greater for larger τ^{1km} with $R_{o=n}$(1-D vho) > $R_{o=n}$(1-D vhe) with "n" the number of scattering order "o," from the second s.o. on. Here and in the remainder, we use the notations

$$R_{o=n} = I_n(\boldsymbol{x}, \boldsymbol{\Omega});$$
$$R_{o>n} = \sum_{i=n+1}^{\infty} I_i(\boldsymbol{x}, \boldsymbol{\Omega});$$
$$R_{o\leq n} = \sum_{i=0}^{n} I_i(\boldsymbol{x}, \boldsymbol{\Omega});$$

and so on, where $\boldsymbol{x}$ is upper boundary point and $\boldsymbol{\Omega}$ a set direction. Thus, for total radiance, R or $R_{tot} = R_{o\geq 0} = R_{o\leq\infty}$. In practice, we took ∞ as 10.

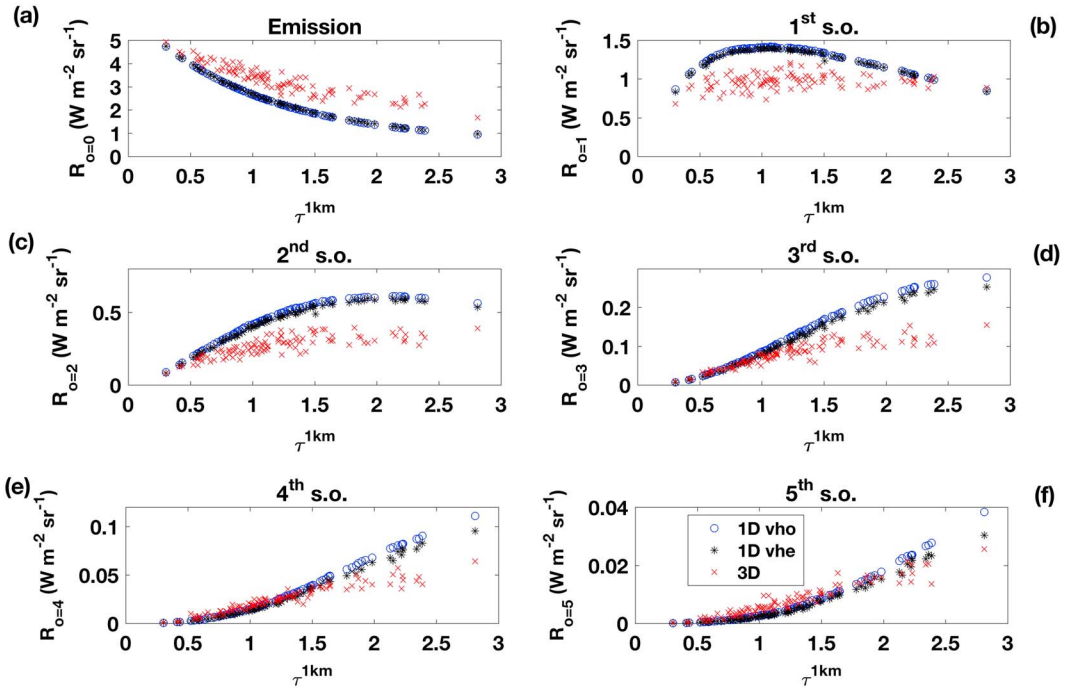

Figure 5. Nadir radiances *R* from the emission order to the fifth s.o., as a function of the optical thickness at 1 km (τ^{1km}) for different cases. One-dimensional vho and 1-D vhe correspond to 1-D RT cases with vertically homogeneous and heterogeneous optical properties, respectively, and 3-D corresponds to a full 3-D RT with heterogeneous 3-D (horizontally and vertically) optical properties. Wavelength is 8.65 μm (most scattering and opaque channel).

On the other hand, we clearly see that the 3-D and 1-D radiances are very different. Concerning the emission order (no scattering nor reflection), 3-D radiances are larger than 1-D radiances and the effect increases with the optical thickness. Indeed, in 1-D, the RT calculation is computed for averaged optical properties, whereas in 3-D, the RT was first performed at the spatial resolution of 100 m before the results were averaged to 1 km. In 3-D, the emission order has larger values than its 1-D counterpart and leads to a larger contribution to the total radiance (as we will see later in Figure 6) due to the PPA bias caused by the nonlinearity of the optical thickness averaging. This effect increases with the pixel optical thickness because the standard deviation of the optical thickness is most often greater in thicker areas (by design in the stochastic 3DCLOUD model). For the next orders of scattering, the 1-D radiances are larger than in 3-D, particularly for optical thickness near unity. Indeed, in 1-D RT, because the optical thickness is horizontally uniform, radiation must, on average, be scattered once or several times before it can reach TOA, whereas in 3-D RT, the near-isotropic thermal radiation can always escape through the "holes" in the extinction field, being the paths of least resistance for the radiation [*Liou and Ou*, 1979; *Harshvardhan and Weinman*, 1982; *Heidinger and Cox*, 1996]. Thus, compared to 1-D RT, 3-D RT will see more direct transmission of the just emitted radiation for a given optical thickness. It will also see less scattered radiance because its source has been depleted due to the aforementioned increased escape rate of nonscattered radiation.

Focusing on the first s.o. in Figure 5b, the 1-D curves have a "frown" shape as a function of the optical thickness from which we can isolate three different regimes.

1. Small optical thicknesses ($\tau^{1km} < 0.5$). The scatterings are very few because the extinction is weak resulting in small radiance values.
2. Medium optical thicknesses ($0.5 < \tau^{1km} < 1.5$). The extinction is large enough to allow a sufficient amount of single scattering without a too large absorption resulting in large radiance values.
3. Large optical thicknesses ($\tau^{1km} > 1.5$). The absorption is strong and decreases the radiance contribution of theses optical thicknesses.

In 1-D, for s.o. larger than 1, radiance contributions to total radiance are smaller for each successive order and the maximum contribution at each s.o. corresponds to the largest optical thicknesses within the present range. The probability of higher orders of scattering is indeed linked to the optical thickness, even if the absorption

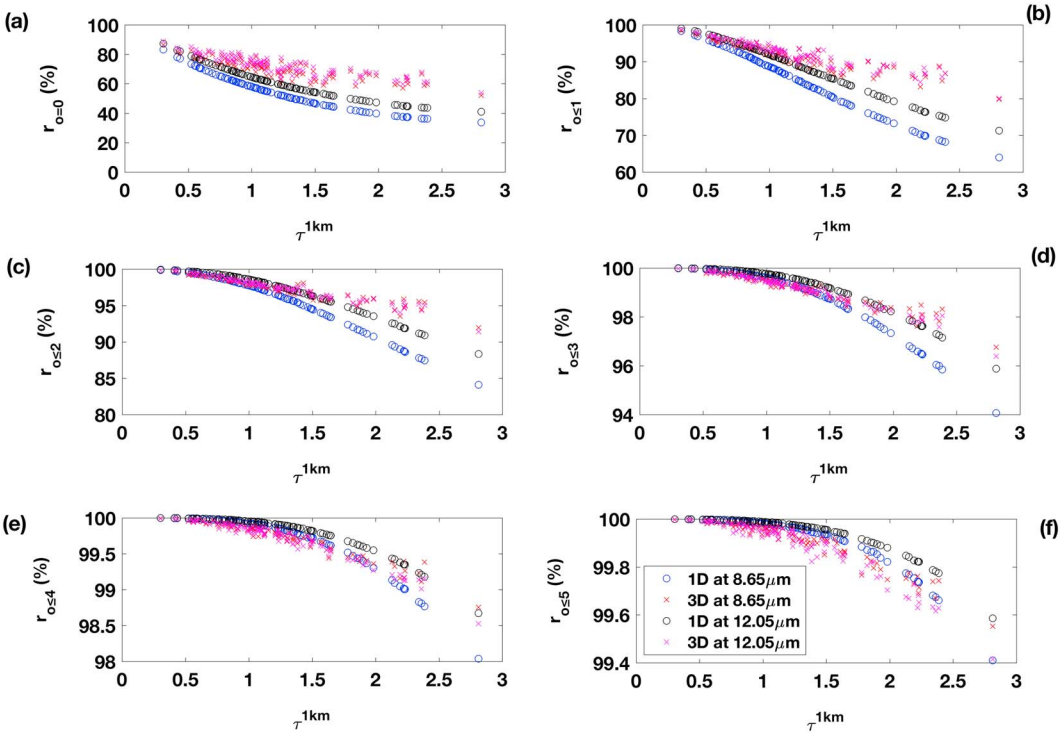

Figure 6. Sum of radiances (R) viewed from nadir, (a–f) from the emission order to the fifth s.o., relative to total radiance (r_o (%) = 100 × $R_{o\leq n}/R$ with R_o and R the radiances at the scattering order o and total, respectively), as a function of the local optical thickness (τ^{1km}) for vertically homogeneous optical properties (1-D vho, circles) and 3-D heterogeneous optical property (3-D, crosses); both bands are represented, 8.65 μm and 12.05 μm.

increases. In 3-D, radiation can cross different cloud columns, having different optical thicknesses, which leads to a more even distribution of their radiance contributions across the range of local optical thicknesses.

Figure 6 shows the percentage of the observed radiance, in 3-D and in 1-D, at each *additional* s.o. relative to total radiance, for bands at 8.65 μm and 12.05 μm. In this case, the contributions of each of the s.o. are summed from the emission to the s.o. n and we plot $100 \times R_{o\leq n}/R$. For the emission order only in Figure 6a, we can see that $R_{o=0}$ are slightly larger (about 3% on average) at 12.05 μm than at 8.65 μm, in both 3-D and 1-D. Indeed, the Planck function is slightly greater at 12.05 μm and the gaseous absorption is larger at 8.65 μm, which both contribute to higher radiances at 12.05 μm. In the 1-D vho configuration used here (since it is amenable to very efficient deterministic evaluation), $R_{o=0}$ is smaller than in 3-D for both bands, because of the averaging effect, already discussed above, leads to more radiant energy coming from the surface directly to the TOA in 3-D. We can also see that, on average, less scattering orders are needed to obtain the total radiance (convergence of the Neumann series in (4) is faster) in 1-D than in 3-D even though the emission $R_{o=0}$ is larger in 3-D; see Figures 6a and 6f. This is likely due to the net horizontal transport effect allowing a larger cloud extinction variability along the path in 3-D leading, on average, to higher-order scatterings before convergence. Therefore, in accordance with Figure 5, the emission order is larger in 3-D than in 1-D, but the scattering contributions are smaller.

Fauchez et al. [2014] show that brightness temperature differences (ΔBT) between 3-D and 1-D are better correlated with the standard deviation of the optical thickness than the optical thickness itself. Therefore, in Figure 7, the radiance differences ($\Delta R_{o=n} = R(\text{3-D})_{o=n} - R(\text{1D})_{o=n}$), from the emission to the fifth s.o. are plotted as a function of StDev$[\tau]^{1km}$, the standard deviation of optical thickness within 1 km areas. As discussed for Figure 5, we first see that $\Delta R_{o=n}$ of the emission ($n = 0$) is positive and is negative for the higher orders of scatterings ($n > 0$) due to the PPA. $\Delta R_{o=n}$ increases in absolute value with StDev$[\tau]^{1km}$, except for the first s.o. in Figure 7b. This is due to the three different regimes for the first scattering order of 1-D radiances already discussed in reference to Figure 5. For the other next s.o., as shown in Figure 5, the individual scattering contributions, which are larger in 1-D, lead to negative $\Delta R_{o=n}$ drop in absolute value with increasing n. However, the probability of scattering increases with the optical thickness of the pixel. For the

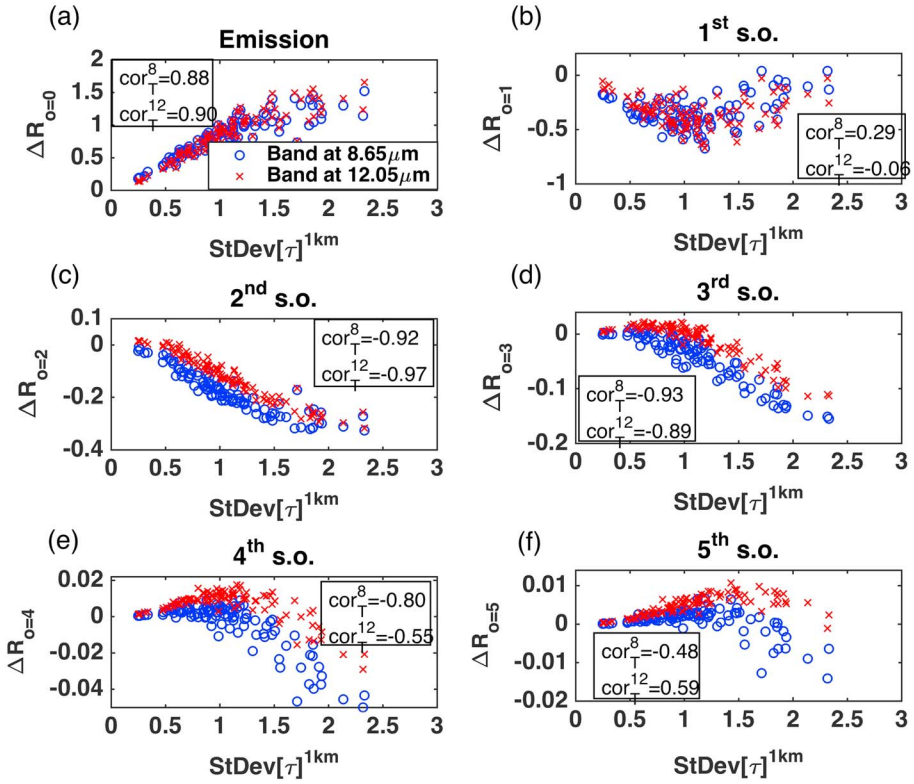

Figure 7. Radiance differences, $\Delta R_{o=n} = R_{o=n}$(3-D) $- R_{o=n}$(1-D), from the emission order to the fifth s.o., nadir view, as a function of StDev[τ]^{1km}, the standard deviation of the optical thickness at 1 km, for the bands at 8.65 μm (blue circles) and 12.05 μm (red crosses).

second s.o., $\Delta R_{o=2}$ decreases almost linearly with StDev[τ]^{1km}, but we can see from the third s.o. that there is virtually no differences ($\Delta R_{o>2} \approx 0$) for small optical thickness standard deviations (also corresponding to small optical thicknesses); see also Figures 5d–5f. Indeed, on the one hand, the number of scatterings for these optical thicknesses is small, and on the other hand, when the s.o. increases, the radiance contribution to the total radiance becomes weaker. Only at large optical thickness variances, where the PPA and IPA biases are both large, lead to significant radiance differences between 3-D and 1-D.

3.2. Differences Between 3-D and 1-D Scatterings for Off-Nadir Viewing

In the previous section, figures and discussions concerned nadir viewing at TOA. In this section, we look at different observation geometries at TOA and their impact on the emission and orders of scatterings. Figure 8 shows 3-D and 1-D radiances, as a function of local optical thickness, for the emission order and for the first to tenth s.o., for several viewing zenith angles ($\Theta = 0°$, 20°, 30°, and 60°) and an azimuth view angle ($\Phi_v = 0°$) for the bands at 8.65 μm and 12.05 μm.

Concerning the emission order (Figures 8a, 8c, 8e, and 8g), $R_{o=0}$, we see that the radiance values, both in 3-D and 1-D, decrease with increasing Θ_v. Indeed, because the optical path through the cloud increases, less and less radiation from the surface or the lowest layers of the cloud is able to cross the cloud without interaction. This decrease is more rapid at small optical thicknesses. For large optical thicknesses ($\tau > 2$), the extinction view from nadir is already important and associated with smaller radiances. Consequently, the increase of the optical path does not change significantly the amount of radiation crossing the cloud (saturation effect). In 3-D RT, with $\Theta_v > 0°$, the observed radiation can cross many cloudy columns with different optical thicknesses, which increases the dispersion of the relation. The largest differences between 3-D and 1-D RT occur at $\Theta_v = 40°$. At larger angles (60°), the absorption is too strong and only the top layers of the cloud, which are colder, matter. This drastically decreases the radiance contribution of large optical thicknesses, smoothing the differences between 3-D and 1-D radiances.

Concerning scattered radiation (Figures 8b, 8d, 8f, and 8h), $R_{1 \le o \le 10}$, we can see that in 3-D, the increase of Θ_v flattens the relation between the radiance and the optical thickness. At $\Theta_v = 60°$, there is almost no variation

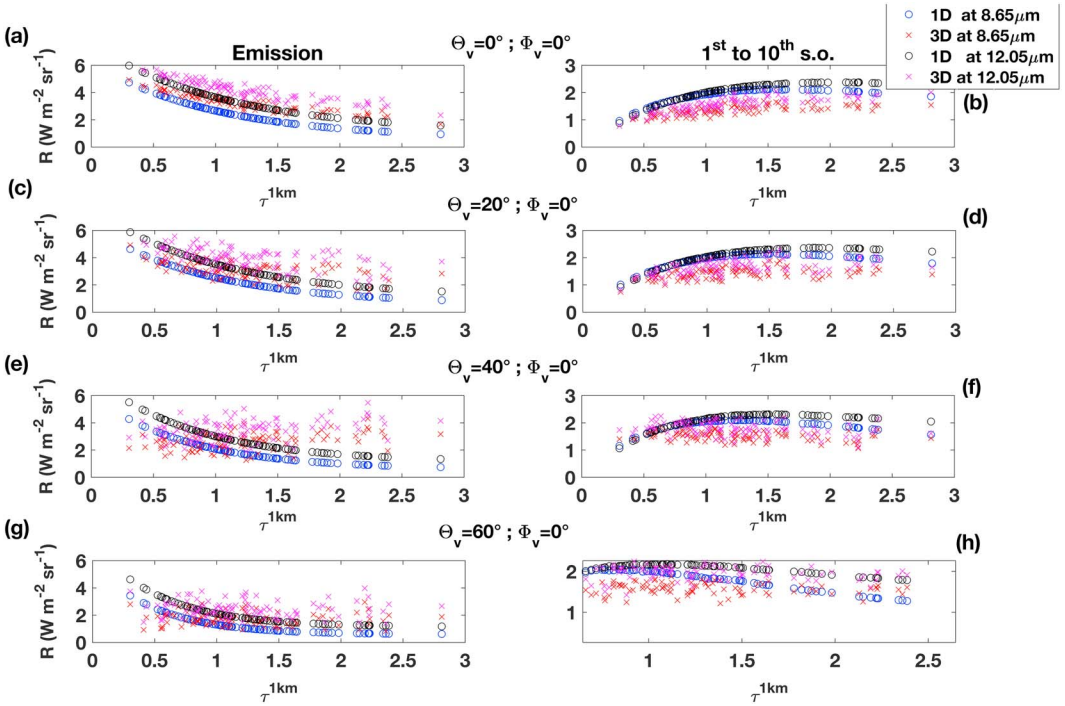

Figure 8. Radiances R (W/m^2/sr), for 3-D and 1-D (vho configuration), (a, c, e, and g) from the emission order, $R_{o=0}$, and (b, d, f, and h) for the sum of the scattering orders 1 to 10, $R_{1\leq o\leq 10}$, as a function of the optical thickness at 1 km ($\tau^{1\text{km}}$) at various viewing zenith angles (Θ_v = 0°, 20°, 30°, and 60°, and Φ_v=0°). Both 8.65 μm and 12.05 μm bands are represented.

between small and large optical thicknesses because the absorption is very large. In 1-D, for large viewing zenith angles, the radiance tends to decrease for large optical thicknesses as the absorption increases. Note that the differences between 3-D and 1-D s.o. contributions to the total radiance are slightly reduced when Θ_v increases because of the increasing absorption and because of the statistical homogenization of optical properties along the line of sight. Note that the azimuth view angle may also impact the differences, due to different crossed optical properties, but these differences are dependent on the particular geometry of the cirrus, and no general conclusion can be drawn. Thus, we do not present the impact of the azimuth view angle in this paper.

4. Approximations of the 3-D RT

4.1. Truncation of the Number of 3-D Scattering Orders

Three-dimensional RT calculations provide realistic radiance fields, but they are very time consuming by comparison with their 1-D counterparts. Indeed, with our Monte Carlo model, 1-D simulations are achieved in about 1 to 2% of the time needed in 3-D. Moreover, deterministic implementations of 1-D (even vector) RT can be executed in a small fraction of that already reduced time. For illustration, the appendix describes a deterministic 1-D RT computation of singly scattered radiance.

In this study, we nonetheless proceed with Monte Carlo 1-D RT for simplicity. The large 3-D to 1-D speed-up in Monte Carlo runtime is due, on the one hand, to the dimensions of the domain and the number of voxels describing it for 3-D ($100\times100\times n_z$, where N_z is the number of layers along the vertical axis, versus $10\times10\times N_z$ for 1-D that is 100 more voxels in 3-D). This, for example, implies that the random sampling of the FLIPs takes place though the 3-D atmosphere and not only in one column as in 1-D and, on the other hand, to the 3-D scattering. Indeed, as the heterogeneity on the FLIP path is larger in 3-D than in 1-D, good statistical accuracy takes longer to achieve.

At any rate, there is always a significant advantage in reducing the timing for calculations in 3-D RT, even if it calls for an approximation with a known cost in accuracy. In Figures 9a and 9c, 3-D total radiances (3-D tot) for bands at 8.65 μm and 12.05 μm are compared to 3-D radiances with only the order(s) of scattering:

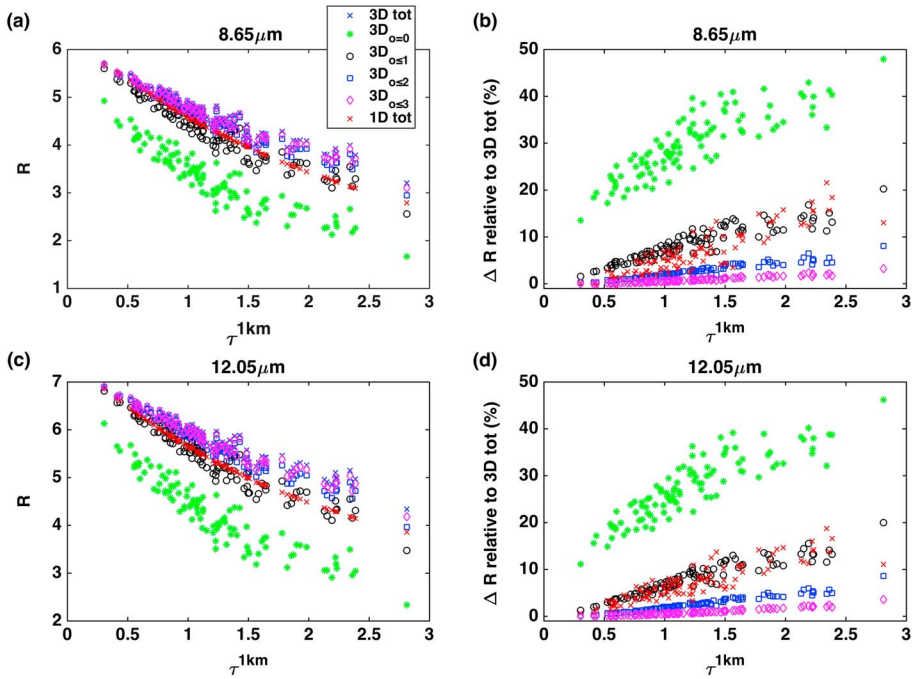

Figure 9. (a and c) Radiances (R) at 8.65 μm and 12.05 μm, respectively, as a function of the optical thickness (τ^{1km}) for a full 3-D RT (3-D tot), 3-D RT with only the scattering order 0 (3-D$_{o=0}$), 0 and 1 (3-D$_{o=1}$), 0, 1, and 2 (3-D$_{o=2}$), 0, 1, 2, and 3 (3-D$_{o=3}$), and a full 1-D RT (1-D tot). (b and d) Relative differences in percent, at 8.65 μm and 12.05 μm, respectively, between the total 3-D radiances and each approximation by successive orders of scattering.

0 (3-D$_{o=0}$); 0 and 1 (3-D$_{o\leq1}$); 0, 1, and 2 (3-D$_{o\leq2}$); 0, 1, 2, and 3 (3-D$_{o\leq3}$); and to total 1-D radiance (1-D$_{tot}$). The relative differences $\Delta R_{o\leq n}$ to total 3-D radiances (Figures 9b and 9d) increase with the optical thickness since the average number of scatterings increases naturally with the optical thickness. We can see that $\Delta R_{o\leq n}$ of the 3-D approximations (by truncating the s.o. at n) are smaller than the 1-D ΔR (for total radiances) for $n \geq 2$. At least carrying the s.o. up to 3 is necessary to see a relative error below 3% in 3-D.

Table 1 summarizes the different cases presented above. Values are averaged over the whole cirrus field and are relative (in %) to the total 3-D radiance. Both radiances and Monte Carlo computation times are compared for successive orders of scattering from 0 to 3 in 3-D and for the total 1-D radiance relative to the total 3-D radiance for bands at 8.65 μm and 12.05 μm.

In 1-D Monte Carlo RT, the calculation time is much smaller (1 and 2% for bands at 8.65 μm and 12.05 μm, respectively) and corresponds to about (94%) of the total 3-D radiance. In 3-D, the time computation increases, obviously, with the orders of scattering included. For three successive scatterings, the CPU time needed is about 90% of the time needed for total radiances. This is not a great improvement, but it can make a difference for some studies. In terms of radiance accuracy, we note that on average the three first s.o. correspond to about 99% of the total radiances. Thus, s.o. larger than 3 contributes weakly to both the total 3-D time computation

Table 1. Radiances Averaged Over the Whole Cirrus Field[a]

	Band (μm)	$\overline{\text{3-D}_{o=0}}$	$\overline{\text{3-D}_{o\leq1}}$	$\overline{\text{3-D}_{o\leq2}}$	$\overline{\text{3-D}_{o\leq3}}$	$\overline{\text{1-D}_{tot}}$
Rad (%)	8.65	73.9	92.6	97.8	99.4	94.6
Time (%)	8.65	39	62	74	89	1
Rad (%)	12.05	76.3	93.2	98.0	99.4	93.9
Time (%)	12.05	69	74	78	92	2

[a] $\overline{\text{3-D}_{o=0}}$, $\overline{\text{3-D}_{o\leq1}}$, $\overline{\text{3-D}_{o\leq2}}$, $\overline{\text{3-D}_{o\leq3}}$, and $\overline{\text{1-D}_{tot}}$ correspond respectively to 3-D RT with only s.o. 0; 0 and 1; 0, 1, and 2; and 0, 1, 2, and 3, while 1-D$_{tot}$ corresponds to a full 1-D RT computation. All the values are given in percent relative to the total 3-D radiance values and to the computer time to compute them.

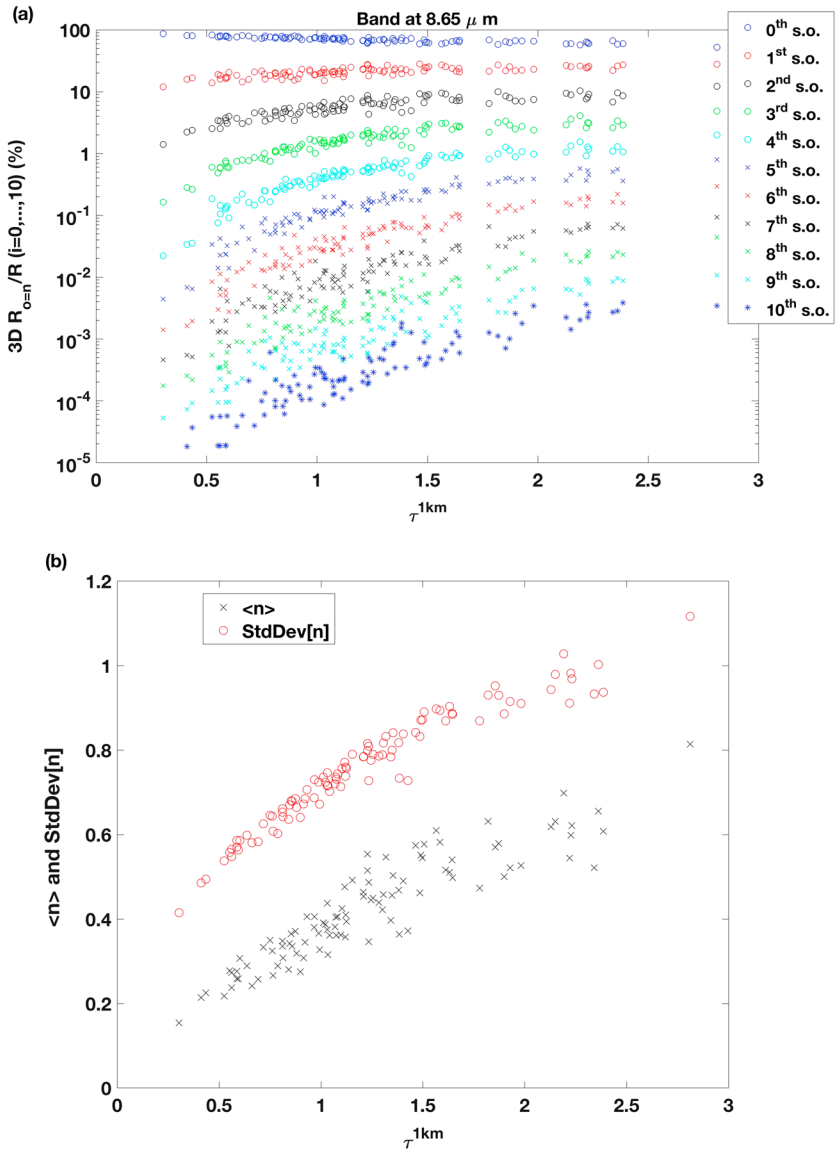

Figure 10. (a) Relative radiance contribution (%) of each scattering order (3-$D_{s.o.}$/3-D_{tot}) as a function of the local optical thickness at 1 km (τ^{1km}). (b) Mean and standard deviation of the s.o. *n* from (6) versus τ^{1km}. The 8.65 μm band is used in both panels.

and the radiance on the whole fields. Note that this relative error estimate is for the average over the whole cirrus field; locally, the relative error depends strongly on the optical thickness.

For a more detailed description of s.o.-truncated computations of 3-D radiances as a function of the optical thickness, we plot in Figure 10a, in log scale, the relative contribution of each s.o. according to the optical thickness for the band at 8.65 μm. For example, to have a precision of about 1%, we need to compute the first two orders of scattering for an optical thickness of 0.5 and the first four orders for an optical thickness of 2.5. Note that we approximate here the relative truncation error for $R_{o\leq n}$ by the relative contribution of $R_{o=n}$ (i.e., $\sum_{o=n+1}^{\infty}(R_o) << R_{o=n}$), which is justified when the Neumann series is quasi-geometric. At a fixed optical thickness, this behavior is visible in the semilog plot in Figure 10a, at least for large *n* and τ^{1km}. Table 1 and Figure 9 indicate that conclusions will be similar for the band at 12.05 μm, although the monotonic decrease to 0 is faster and, consequently, the mean and dispersion of *n* are smaller.

To summarize, we have seen that if we assume that the 3-D RT can be limited to the third s.o. for an accuracy of about 1%, then we save about 10% of the Monte Carlo computation time, which can be appreciable for

multiple runs (e.g., several bands or cirrus cases). However, the accuracy is smaller for large optical thicknesses where around 96 to 97% of the total radiance is obtained by $R_{\leq 3}$ because the contribution of greater s.o. is more important. In the next section, we develop a parameterization to improve the approximation of the 3-D RT for large optical thickness.

A simpler way of quantifying the role of scattering in cirrus in this spectral region is to compute the first couple of moments of the decomposition of R according to n, that is,

$$\langle n^q \rangle = \frac{1}{R} \sum_{n=0}^{\infty} n^q R_{o=n}, \tag{6}$$

where $R_{o=n}/R$ is the probability of scattering exactly n times from emission to detection. We also recall that in this study, ∞ is identified as 10. In Figure 10b, we plot the mean $\langle n \rangle$ (i.e., $q = 1$ in the above) and the standard deviation, $\sqrt{\langle n^2 \rangle - \langle n \rangle^2}$, of the discrete random variable n as a function of $\tau^{1\text{km}}$. As expected, $\langle n \rangle$ increases steadily with the local opacity of the cirrus. However, even in the most opaque regions, with $\tau^{1\text{km}} > 2$, $\langle n \rangle$ barely exceeds 0.5 on average. This means, on the one hand, that $n = 0$ (direct emission) still dominates the thermal radiation transport to TOA and, on the other hand, that $n = 1$ (single scattering) dominates the scattered radiation. Finally, we note that the standard deviation of n remains $\approx$2 times its mean value. This tells us that there may be a way of predicting the contribution of higher-order scattering from the lowest orders that dominate $\langle n \rangle$ across the whole range of $\tau^{1\text{km}}$ in cirrus. We will capitalize on these remarks further in the design of a fast 3-D RT model for estimating TIR radiances from cirrus.

4.2. Presentation of the Hybrid Model

In this section, we present a special 3-D RT approximation model that we call "hybrid" because it uses a parameterization with both partial 3-D and partial 1-D computations to estimate the full 3-D RT in a potentially very short computation time at any cirrus optical thickness in the range explored here.

In section 4.1, we saw that the direct 3-D emission ($3\text{-D}_{o=0}$) contribution dominates the total radiance: 73.9 and 76.3% for bands at 8.65 μm and 12.05 μm, respectively, over the whole domain. Although our estimates are Monte Carlo based, we know that it can be quickly calculated analytically by using precomputed sweeps through the 3-D grid that generates arrays of partial paths that intersect specific voxels. Moreover, the contribution of the scattered radiance comes mainly from the first s.o., and other orders contribute only to about 7% of the total radiance and are dependent on the optical thickness.

We propose to approximate 3-D total radiance by adding to the direct 3-D emission term ($3\text{-D}_{o=0}$) the first s.o. from 1-D ($1\text{-D}_{o=1}$) along with a parameterization to account for the contributions from s.o. >1. Specifically, we assume that the sum of these higher scattering orders increases linearly with the optical thickness, as already seen in Figure 5. The mathematical form of the hybrid model is then

$$3\text{-D}_{\text{tot}} \approx 3\text{-D}_{o=0} + 1\text{-D}_{o=1} + 1\text{-D}_{o=1} \times \left(a\,\tau^{1\text{km}} + b\right), \tag{7}$$

with coefficients a and b to be determined by regression.

In order to use this hybrid model (named here as "H1") on arbitrary cirrus fields, we have to determine the dimensionless parameters (a, b) of the first degree polynomial $y = ax + b$, with $x = \tau^{1\text{km}}$. From (7), we have

$$y = \frac{3\text{-D}_{\text{tot}} - 3\text{-D}_{o=0}}{1\text{-D}_{o=1}} - 1. \tag{8}$$

We determined numerically parameters a and b by first-order polynomial (i.e., linear) regression based on the 3-D_{tot} nadir data presented above. Values of these two parameters are shown in Table 2. We also estimated these parameters for different parts of the field (half or quarter field), and their values are very close whatever the part of the cirrus is considered.

Figure 11a illustrates the quality of the fit of y in equation (8) versus $\tau^{1\text{km}}$, by which (a, b) are determined. This procedure ensures that our hybrid H1 model fits the 3-D total radiance data with optimal agreement. Specifically, the "R-squared" correlation coefficient of the regression is better than 0.90 and the RMSE is smaller than 0.15 W/m^2/sr for both TIR channels. In Figure 11b, we plot 3-D total radiances and the results of the hybrid model as well as 1-D total radiances for 8.65 μm and 12.05 μm bands. As expected, the distributions of hybrid model points are close to those of the total 3-D radiance, although a little more dispersed.

Table 2. Dimensionless Parameters a and b of the Linear Adjustment Function ($a\tau^{1km} + b$) Used in the Hybrid 3-D RT Model (7) to Account for Multiple Scattering and 3-D RT Effects[a]

Parameters	a	b
Band at 8.65 μm	0.325	−0.357
Band at 12.05 μm	0.267	−0.245

[a]The IIR/CALIPSO spectral bands at 8.65 μm and 12.05 μm are considered. We note that $a+b \approx 0$, which means that the correction is negligible where $\tau^{1km} = 1$, and this is indeed the expected crossing line from single- to multiple-scattering regimes.

We note in passing that a similar parameterization of the s.o. makeup of 3-D radiance is not possible for the solar spectrum where the radiance *e*-folding scale for scattering is much longer, and the neighboring pixels' influence is much stronger. We note, however, that a method similar to ours was proposed by *Gabriel and Evans* [1996] for solar radiation but limited to 2-D RT in simplified heterogeneous media and targeting only domain-average fluxes (as opposed to our pixel-scale radiances).

We have thus shown that 3-D radiances can be well approximated (with 0.15 W/m^2/sr RMSE) by a hybrid model based on the 3-D direct emission, the 1-D first s.o., and an adjustment to account for higher orders of scattering using an empirically determined linear function of optical thickness. In addition, the computational time is drastically reduced since we need only to calculate analytically the direct emission by using precomputed sweeps through the 3-D grid and to run 1-D RT simulations for other scatterings orders.

4.3. Evaluation of the Hybrid Model

To estimate the general applicability of the H1 model to arbitrary 3-D cirrus fields, we test it on a completely different one (namely, "cirrus 2"). This new cirrus field is based on the AFGL-TR-86-0110 [*Anderson*, 1986] mid-latitude summer meteorological profile. Figure 12 shows the optical thickness (a) and the IWC (b) of cirrus 2.

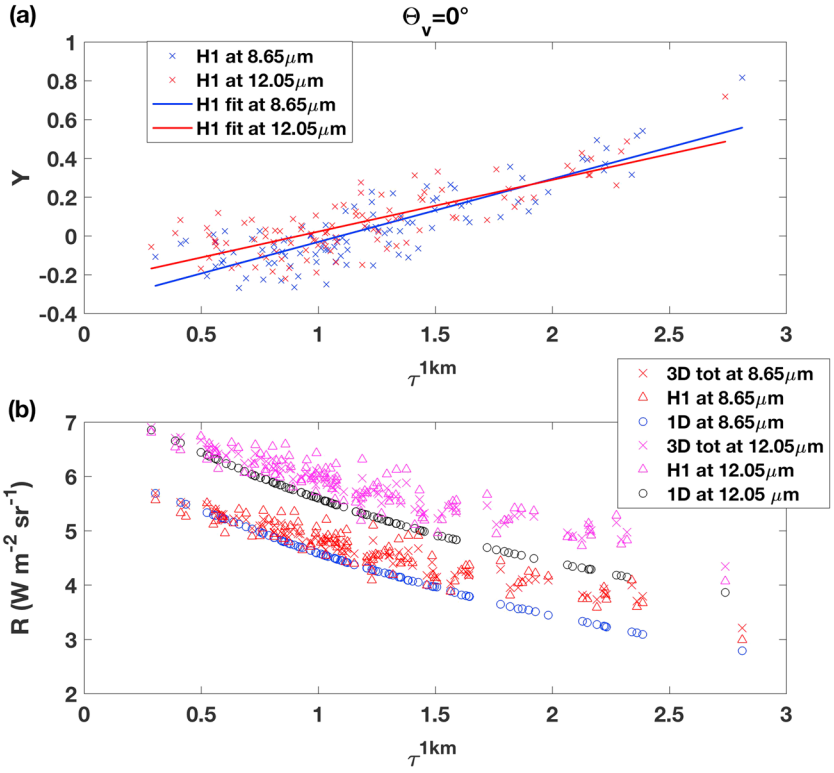

Figure 11. (a) Y values in (8) versus τ^{1km} at 8.65 μm and 12.05 μm for the nadir view of cirrus 1; also shown is the $a\tau + b$ adjustment term in (7), as determined by linear fit. (b) Three-dimensional total radiances, H1 hybrid model, and 1-D total radiance model.

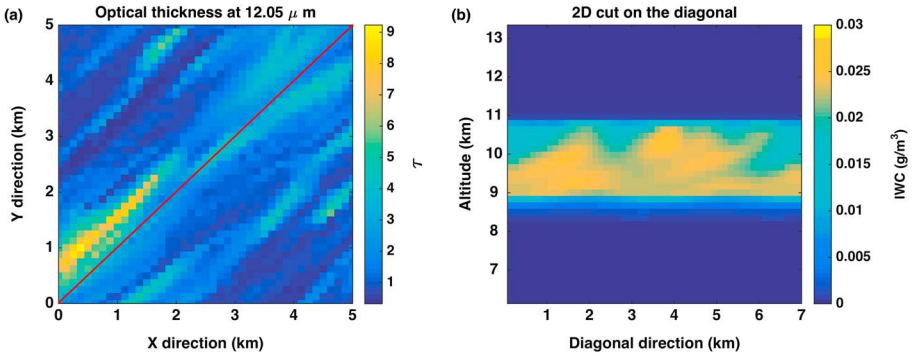

Figure 12. (a) Optical thickness (τ) at 12.05 μm of the 5×5 km^2 cirrus 2 field and (b) diagonal transect of the IWC corresponds to the red line in Figure 12a. Mean optical thickness $\bar{\tau} = 1.8$, and its heterogeneity parameter $\rho_\tau = 0.5$.

Table 3 summarizes the physical parameters between the previous and new cirri, showing that the two clouds are quite different.

In section 3.1, we showed that the impact of vertical variability of optical properties on the TOA radiances is negligible by comparison to horizontal heterogeneity. For this new cirrus field we used a different optical property parameterization by *Yang et al.* [2005]. We considered a unique aggregate column crystal shape with an effective diameter D_{eff} of 20 μm in the entire cirrus. This ice crystal model is used in the IIR retrieval algorithm [*Garnier et al.*, 2013]. The selection of aggregate columns for RT simulation in the TIR instead of other shapes considered in the IIR retrieval algorithm (namely, solid column and plate) is based on the study of *Holz et al.* [2016], who found that the use of aggregated columns in the IR split-window technique provides the more consistent cloud optical thickness retrievals when compared with lidar and visible and near-/shortwave-/midwave-infrared (VNIR/SWIR/MWIR) retrievals. Different RT simulations are performed for both 8.65 μm and 12.05 μm bands:

1. Three-dimensional RT
   a. full 3-D RT (3-D$_{\text{tot}}$)
   b. 3-D RT only for the direct emission (3-D$_{o=0}$)
2. One-dimensional RT
   a. full 1-D RT (1-D$_{\text{tot}}$)
   b. 1-D RT only to the first s.o. (1-D$_{o\leq 1}$)

In order to use the hybrid model on this new cirrus field, we modify equation (7) to account for changes in the scattering properties between the two cirrus field:

$$\text{3-D}_{\text{tot}} \approx \text{3-D}_{o=0} + \text{1-D}_{o=1} + \text{1-D}_{o=1} \times \left(a \times c \times \tau^{1\text{km}} + b\right), \tag{9}$$

with coefficients a and b already determined by regression for the first cirrus case (see Table 2) and coefficient c is $[(1-g_2)\varpi_{0,2}]/[(1-g_1)\varpi_{0,1}]$ with the indices 1 and 2 designate cirrus 1 and cirrus 2 cases, respectively. The c formulation comes from the similarity principle of the two stream approximation [*van de Hulst*, 1974;

Table 3. Comparison of the Cloud Parameters of Cirrus Models 1 and 2: Average Extinction Coefficient σ_e, Single Scattering Albedo ϖ_0, and Asymmetry Parameter g at 8.65 μm and 12.05 μm, $\bar{\tau}$ and ρ_τ Values Are for the Band at 8.65 μm Only, CBA and CTA Correspond to Cloud Base Altitude and Cloud Top Altitude Respectively

Parameters	$\overline{\sigma_e}$	$\overline{\varpi_0}$	$\bar{g}$	$\bar{\tau}$	ρ_τ	CBA	CTA	Field Size
8.65 μm band	(1/km)	(–)	(–)	(–)	(–)	(km)	(km)	(km^2)
cirrus 1	0.83	0.57	0.94	1.2	0.4	7.5	8.9	10×10
cirrus 2	2.46	0.75	0.94	1.8	0.5	10.9	11.9	10×10
12.05 μm band	(1/km)	(–)	(–)	(–)	(–)	(km)	(km)	(km^2)
cirrus 1	0.81	0.50	0.91	1.2	0.4	7.5	8.9	10×10
cirrus 2	1.95	0.47	0.93	1.4	0.4	10.9	11.9	10×10

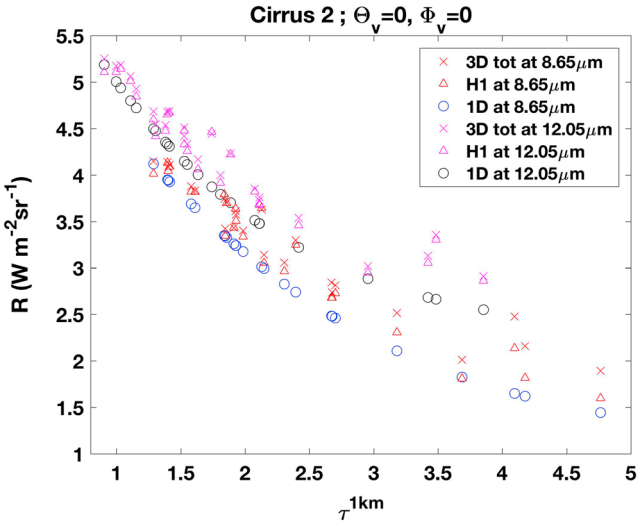

Figure 13. Three-dimensional total radiance (3-D tot), hybrid model (H1), and 1-D total radiance (1-D tot) at 8.65 μm and 12.05 μm for the alternative cirrus field in Figure 12.

Twomey et al., 1986] and is equal to 1 in the cirrus 1 case. Because *a* and *b* coefficients were determined in the cirrus 1 case, the similarity relationship allows a normalization of the scattering properties of any other cirrus case to the cirrus 1 case. Figure 13 shows 3-D_{tot} and 1-D_{tot} radiances along with predictions of the H1 model for the 8.65 μm and 12.05 μm bands. We can see that agreement between 3-D_{tot} and the H1 model is good for both bands ($R^2 = 0.95$; RMSE = 0.14 and $R^2 = 0.99$; and RMSE = 0.07 for bands at 8.65 μm and 12.05 μm, respectively), even if the differences slightly increase for large optical thicknesses at 8.65 μm. Indeed, for this band, the scattering is larger than at 12.05 μm and the approximation of the hybrid model is less accurate but still better than the 1-D simulation.

5. Conclusions and Outlook

We show how cirrus cloud heterogeneities (vertical and horizontal) impact the direct emission (from clouds, atmosphere, or surface) as well as the scattered thermal radiation according to order. We also present an efficient computational model to approximate the 3-D radiative transfer using a combination of 3-D transport without scattering and scattering based on analytic 1-D theory with an empirical adjustment for higher orders and 3-D effects. Two different cirrus clouds are modeled with the 3DCLOUD code [*Szczap et al.*, 2014] with their optical thickness wave number spectrum following a power law with exponent −5/3 from 100 m to the outer scale of 10 km (the size of the domain). The effects of the power law exponent on the 3-D TIR RT have not been estimated here but will be the subject of a future work. The 3-D radiative transfer is simulated with the 3DMCPOL [*Cornet et al.*, 2010; *Fauchez et al.*, 2014] code for the two thermal infrared channels at 8.65 μm and 12.05 μm of the Imaging Infrared Radiometer (IIR) on the CALISPO satellite. This Monte Carlo scheme is well suited for investigating numerically the composition of observed radiance by orders of scattering.

We first show that the vertical heterogeneity impact on radiances, for both the direct emission and scattered radiation, is negligible by comparison with horizontal heterogeneity effects. For nadir view and direct emission, 3-D radiances are larger than 1-D counterparts, and this difference increases with the pixel heterogeneity due to the PPA bias. More generally, the underestimation of the surface emission caused by the PPA bias increases as spatial resolution decreases (pixel size increases). By contrast, concerning the scattered radiation, radiances are smaller in 3-D than in 1-D because, in the former case, most of the radiation has already crossed the cloud as direct emission. The first scattering order still has a significant contribution to the 3-D to 1-D difference ΔR, and three different regimes occur as a function of $\mathrm{StDev}[\tau]^{1\mathrm{km}}$. For higher orders, the number of scatterings increases almost linearly with the optical thickness over the range covered in cirrus. For off-nadir-viewing geometries, ΔR, on average, increases as a function of the viewing zenith angle for emission, due to the increasing difference between 1-D and 3-D optical paths, but slightly decreases for scattered radiation. Since cirrus are highly anisotropic in space, azimuthal view angle may also impact the differences

for the same reason. This could be the subject of future study. Here we used an azimuthal direction that was neither aligned nor at right angles with the direction along which the cirrus are spread out.

Monte Carlo codes are intuitive and elegant methods to simulate the radiative transfer. They are, however, very time consuming. We show that by limiting the thermal 3-D RT in cirrus to only three cloud scatterings, we can save about 10% of the computation time while 99% of the 3-D radiance is reached, but this is an average value over the whole domain. The percentage is smaller for large optical thicknesses (about 96 to 97%) where the contribution of higher orders is more important.

However, to process thermal images from satellite sensors, we need a much faster forward model, precluding Monte Carlo techniques. Therefore, to estimate 3-D thermal radiance fields across any reasonable range of optical thicknesses in cirrus clouds, we have developed an approximate but highly efficient hybrid (3-D/1-D) model. The total 3-D radiance is estimated by taking the direct 3-D emission, which can be computed using a rapid sweep through the arbitrary 3-D gridded extinction field, and then adding to it the first scattering order from 1-D theory and finishing with a simple empirical parameterization to account for higher orders and 3-D effects. This parameterization assumes a linear dependence on the local optical thickness and fits well the total 3-D radiances for our first cirrus model. As a test, we use the same two coefficients to predict radiances for another cirrus model for channels at 8.65 μm and 12.05 μm. Good agreement between 3-D total radiance and the hybrid model is again found, even if notable differences appear at 8.65 μm for the largest optical thickness values. Our hybrid (3-D/1-D) model is thus a good approximation of the 3-D RT. It can be confidently extrapolated to other thermal infrared wavelengths. Calculation time for the hybrid model is now dependent on 1-D calculation time of the first scattering order only, which can be achieved with an analytical 1-D model or any 1-D radiative transfer model much faster than a Monte Carlo counterpart, thus allowing drastic reduction in computational time with respect to the 3-D full RT.

Although our numerical investigations were conducted entirely with a Monte Carlo code for simplicity, it is straightforward to implement the new hybrid model with very fast deterministic code. We plan to write such code that we will call Fast Algorithm for Three-dimensional Thermal Infrared Radiance Estimation in Cirrus (FATTIRE-C), as described in the appendix. In particular, precomputed voxel-level segment lengths can be used to reduce the 3-D grid sweep to a weighted sum of specific array elements for the extinction field. In the near future, we will achieve the ultimate speed-up by using vertically homogenized profiles in 1-D computations, thus leading to closed-form analytic expressions for the single-scattering contribution.

We will thus have in hand an efficient forward model for computing full-blown imagery of cirrus in the thermal IR at ~1 km resolution. Moreover, this satellite signal prediction model is readily linearized with respect to all the optical properties, gridded or global. If multiangle TIR data becomes available, 3-D tomographic reconstruction of cirrus clouds may thus become feasible following the nonlinear least squares approach used by *Aides et al.* [2013] for a very large number of unknowns describing 3-D aerosol fields. We have no illusions about the challenges that lay ahead: needs for the best possible initial guess and likely also for customized regularization to navigate the inherent ill-posedness. Another potential application for the hybrid FATTIRE-C model may be in accounting for the 3-D spatial variability of water vapor in signals from existing single-view TIR sensors (e.g., AIRS and IASI).

Appendix A: Deterministic Formulation of the Hybrid FATTIRE-C Model

We describe our efficient but approximate model in equation (7) for 3-D RT in cirrus cloud at TIR wavelengths that explicitly predicts TOA radiances. It is implemented in three additive steps: (1) compute the directly transmitted radiation using the given 3-D gridded optical properties, (2) compute the once-scattered radiation assuming the independent pixel approximation, and (3) add a correction using the outcome of (2) and the local optical thickness that accounts for the high orders of scattering. Step (2) has two variants: (2a) constant optical properties, variable temperature, and (2b) isothermal medium. Step (3) is described at length in the main text. We focus here on steps (1) and (2a), leaving (2b), which has the advantage of being analytically tractable, for a future publication.

A1. Definitions

The cirrus cloud is defined on a finite 3-D grid with cells that are uniformly spaced in the horizontal plane (we can think of these as pixels) and arbitrarily spaced in the vertical direction, but in the same way for all pixels.

Grid cells or "voxels" are thus identified by three indices (i_x, i_y, i_z) with $0 \le i_x < N_x$, $0 \le i_y < N_y$, and $0 \le i_z < N_z$. To locate the cell in physical space, its center is at coordinates:

$$(x, y, z)^{\mathsf{T}} = \left((i_x + 1/2)\ell_x, (i_y + 1/2)\ell_y, [z_{\mathrm{g}}(i_z + 1) + z_{\mathrm{g}}(i_z)]/2\right)^{\mathsf{T}}$$

where (ℓ_x, ℓ_y) are the fixed horizontal grid constants and the array $z_{\mathrm{g}}(\cdot)$ contains the $N_z + 1$ vertical grid points, starting at $z_{\mathrm{g}}(0) = 0$ and ending at $z_{\mathrm{g}}(N_z + 1) = z_{\mathrm{TOA}}$, typically the top of the simulated cirrus layer. The discretized cloud model is defined by three fields: extinction $\sigma_{\mathrm{e}}(i_x, i_y, i_z)$ in km^{-1}, single-scattering albedo $\varpi_0(i_x, i_y, i_z)$, and vertically varying absolute temperature $T(i_z)$ in K. There is also a given 2-D array storing the surface emissivity map $\epsilon(i_x, i_y)$. Lastly, we are given surface temperature T_s, which need not be equal to $T(0)$.

A2. Directly Transmitted Radiance for the Given 3-D Medium

The problem here is to compute the first term in both lines of equation (1). To efficiently compute an image, we will us a single ray per pixel, which we will assume are registered to the ground ($z = 0$). The origin of this ray is taken to be the center of each pixel

$$\mathbf{x}_0(i_x, i_y) = (x_0, y_0, z_0)^{\mathsf{T}}(i_x, i_y) = \left((i_x + 1/2)\ell_x, (i_y + 1/2)\ell_y, 0\right)^{\mathsf{T}}.$$

The ray starts at $\mathbf{x}_0$ and is directed toward an above-cloud sensor in direction

$$\mathbf{\Omega} = (\eta \cos\phi, \eta \sin\phi, \mu)^{\mathsf{T}}$$

where $0 < \mu \le 1$, $\eta = \sqrt{1 - \mu^2}$, and $-\pi < \phi \le \pi$. It is relatively straightforward in computational geometry to determine that the half-line

$$\{\mathbf{x} \in \mathbb{R}^3; \mathbf{x} = \mathbf{x}_0 + s\mathbf{\Omega}, s \ge 0\}$$

intercepts $N_{\mathbf{\Omega}} \ge N_z$ cells at $i_{x\mathbf{\Omega}}(j)$, $i_{y\mathbf{\Omega}}(j)$, and $i_{z\mathbf{\Omega}}(j)$ where $1 \le j \le N_{\mathbf{\Omega}}$, which is surely also $\le N_x + N_y + N_z$. Appropriate translations in (i_x, i_y) are applied to scan the whole image, with periodic boundary conditions applied as needed. Each of these voxels is traversed by a segment of length $s_{\mathbf{\Omega}}(j)$ with $1 \le j \le N_{\mathbf{\Omega}}$.

The radiance directly transmitted to TOA is then given by

$$I_{0\mathbf{\Omega}}(i_x, i_y) = \sum_{j=1}^{N_{\mathbf{\Omega}}} \sigma_{\mathrm{a}}(j) I_{\mathrm{bb}}(j) \exp[-\tau_{\mathrm{TOA}}(j)] s_{\mathbf{\Omega}}(j), +\mathrm{surface\_term} \tag{A1}$$

an "upwind sweep," where

$$\sigma_{\mathrm{a}}(j) = \left[1 - \varpi_0(i_{x\mathbf{\Omega}}(j), i_{y\mathbf{\Omega}}(j), i_{z\mathbf{\Omega}}(j))\right]\ \sigma_{\mathrm{e}}\left(i_{x\mathbf{\Omega}}(j), i_{y\mathbf{\Omega}}(j), i_{z\mathbf{\Omega}}(j)\right),$$

$$I_{\mathrm{bb}}(j) = B[T(i_{z\mathbf{\Omega}}(j))],$$

and

$$\tau_{\mathrm{TOA}}(j) = \sum_{i=j+1}^{N_{\mathbf{\Omega}}} \sigma_{\mathrm{e}}(i) s_{\mathbf{\Omega}}(i) + \sigma_{\mathrm{e}}(j) s_{\mathbf{\Omega}}(j)/2.$$

The last quantity is simply the *reverse* cumulation of $[\sigma_{\mathrm{e}}(j)s_{\mathbf{\Omega}}(j) + \sigma_{\mathrm{e}}(j-1)s_{\mathbf{\Omega}}(j-1)]/2$ starting with $\sigma_{\mathrm{e}}(N_{\mathbf{\Omega}})s_{\mathbf{\Omega}}(N_{\mathbf{\Omega}})/2$ Finally, we have

$$\mathrm{surface\_term} = \epsilon(i_x, i_y) B(T_s) \exp\left[-\left(\tau_{\mathrm{TOA}}(1) + \sigma_{\mathrm{e}}(1) s_{\mathbf{\Omega}}(1)/2\right)\right],$$

which completes the computation of 3-$\mathrm{D}_{o=0}$ in equation (7).

Note that the 3-D spatial structure of the cloud will generally leave an imprint on the azimuthal dependence of the nonscattered radiance $I_{0\mathbf{\Omega}}(i_x, i_y)$ in (A1).

A3. Once-Scattered Radiance for a Medium With a Height-Dependent Temperature Profile

We now need to estimate as efficiently as possible 1-$D_{o=1}$ in equation (7) using only optical properties derived from pixel (i_x, i_y) and from the discretized atmospheric column above it.

We are given the surface emissivity $\epsilon(i_x, i_y)$ and surface temperature T_s. So the isotropic incoming radiance at the bottom of the atmosphere is $I_s(i_x, i_y) = \epsilon(i_x, i_y)B(T_s)$, irrespective of entry direction $\mathbf{\Omega}(\mu, \phi)$.

It is always straightforward to estimate the total optical thickness of the atmospheric column at each pixel:

$$\tau_{\text{tot}}(i_x, i_y) = \sum_{i_z=0}^{N_z-1} \sigma_{\text{e}}(i_x, i_y, i_z)\ell_z(i_z) \tag{A2}$$

where $\ell_z(i_z) = z_{\text{g}}(i_z + 1) - z_{\text{g}}(i_z)$.

Here we have a constant extinction, scattering, and absorption coefficients $(\overline{\sigma_{\text{e}}}, \overline{\sigma_{\text{s}}}, \overline{\sigma_{\text{a}}})$ and constant phase function $P(\mathbf{\Omega} \cdot \mathbf{\Omega}')$, where $\mathbf{\Omega}'$ is the incoming direction. Although there are sometimes better choices, they can be taken to be column averages. At any rate, we have

$$\tau_z = \overline{\sigma_{\text{e}}} \times (z_{\text{TOA}} - z),$$

from which we obtain $T(\tau_z) = T(z_{\text{TOA}} - \tau_z/\overline{\sigma_{\text{e}}})$.

From equations (A1)–(A3), the azimuthally independent singly scattered or reflected radiance at the TOA is, under these assumptions,

$$I_1(\tau_{\text{tot}}, \mu) = \int_0^{\tau_{\text{tot}}} S_1(\tau_z, \mu) \exp(-\tau_z/\mu) \mathrm{d}\tau_z/\mu + F_0^{(\text{dn})}(\tau_{\text{tot}})\alpha \frac{\mu}{\pi} \exp(-\tau_{\text{tot}}/\mu) \tag{A3}$$

where we have dropped the explicit (i_x, i_y) dependences for simplicity. We also note that in contrast with nonscattered radiance, there is no azimuthal dependence here since the medium is rotationally and translationally invariant in the horizontal plane, and sources are isotropic. In particular, this means that we only need to know the zeroth-order Fourier component $\overline{P_0(\mu, \mu')}$ of $P(\mathbf{\Omega} \cdot \mathbf{\Omega}')$.

The first term in (A3) is the contribution of radiation scattered in the cloud volume. The optical depth from TOA to altitude z is denoted τ_z and is simply the partial sum in (A2) starting at $i_z > 0$ with linear interpolation inside the $(i_z - 1)^{\text{th}}$ cell as needed. It also calls for $S_1(\tau_z, \mu)$, the order-1 source function, namely,

$$S_1(\tau_z, \mu) = \frac{\varpi_0}{2} \int_{-1}^{+1} \overline{P_0(\mu, \mu')} I_0(\tau_z, \mu') \mathrm{d}\mu', \tag{A4}$$

where ϖ_0 is taken to be $\overline{\sigma_{\text{s}}}/\overline{\sigma_{\text{e}}}$, $I_0(\tau_z, \mu)$ is directly transmitted radiance at optical depth τ_z as a function of μ. For upwelling ($\mu \geq 0$) radiation, it is defined as

$$I_0(\tau_z, \mu) = \int_{\tau_z}^{\tau_{\text{tot}}} \left[1 - \varpi_0(\tau_z')\right] B\left[T(\tau_z')\right] \exp\left[-\left(\tau_{\text{tot}} - \tau_z'\right)/\mu\right] \mathrm{d}\tau_z'/\mu + \epsilon B(T_{\text{s}}) \exp[-(\tau_{\text{tot}} - \tau_z)/\mu] \tag{A5}$$

and computed as

$$I_0(\tau_z, \mu) \approx (1 - \varpi_0) \sum_{i_z=0}^{n_z(\tau_z)-1} B[T(i_z)] \exp[-(\tau_{\text{tot}} - \tau_z)/\mu]\ell_z(i_z)/\mu + \text{interpolation\_term for cell number } n_z(\tau_z) + \text{surface\_term}$$

where $n_z(\tau_z)$ is the value of i_z for the level that contains τ_z, and surface_term = $\epsilon B(T_{\text{s}}) \exp[-(\tau_{\text{tot}} - \tau_z)/\mu]$. For downwelling ($\mu < 0$) radiation, we use $|\mu|$ rather than μ, the integration bounds are 0 and τ_z, so the sum goes from $n_z(\tau_z) + 1$ to N_z, the transmittance becomes $\exp(-\tau_z/|\mu|)$, and the surface_term vanishes. The angular integration in (A4) can be carried out with any convenient quadrature rule. Since all thermal sources are isotropic, we anticipate only mildly anisotropic radiance fields in all but the layers nearest to cloud top/TOA. If only a few spherical harmonics are needed to describe it, then the angular integral in (A4) can be efficiently performed with spherical harmonics.

The second term in (A3) is the contribution of a single surface reflection, with surface albedo $\alpha = 1 - \epsilon$; μ/π is the phase function for a Lambertian surface, and $F_0^{(\mathrm{dn})}(\tau_{\mathrm{tot}})$ is the downwelling hemispherical flux at the surface, namely,

$$F_0^{(\mathrm{dn})}(\tau_{\mathrm{tot}}) = 2\pi \int_{-1}^{0} I_0(\tau_{\mathrm{tot}}, \mu)|\mu|\mathrm{d}\mu. \tag{A6}$$

Here again, the angular integration of $I_0(\tau_z, \mu)$ requires a choice of quadrature rule. Yet here again, it may be advantageous to use spherical harmonics.

That completes the computation of 1-$D_{o=1}$ in equation (7) when T varies (piecewise constant) with height using straightforward numerical methods as needed for interpolation and quadrature in space and angle. So far, we have just replaced the Monte Carlo (MC), aka "random quadrature," approach by a deterministic one to gain efficiency, with one small difference: only one ray from the pixel center is used here, while a backward MC scheme will start many paths at random inside each pixel. That minor difference can be reduced efficiently by starting the deterministic rays at pixel corners and using the average over its four corners to estimate the pixel's mean radiance. Alternatively, one can simply refine the sampling of the pixel from a single ray to 4, 9, etc., on a regular subpixel grid, but the computational cost will increase linearly with the number of rays per pixel.

A4. Optional Above-Cloud and Below-Cloud Absorbing Layers

The above numerical model for thermal 3-D RT in cirrus can be generalized to a whole atmospheric column with absorption by a tenuous gaseous (no scattering nor emission) below and/or above the cloud. First, we assign finite absorption optical thicknesses $\tau_a^{(\mathrm{below})}$ and $\tau_a^{(\mathrm{above})}$. Both should be relatively small since we neglect the associated emission rate $\sigma_a(z)B[T(z)]$ throughout these extra layers. Then

1. $\tau_a^{(\mathrm{below})}$ is used in four ways, as dictated by the transport physics:
   a. to reduce the amount of radiation emitted by the surface that reaches the sensor directly, therefore multiply the surface term in (A1) by $\exp[-\tau_a^{(\mathrm{below})}/\mu]$;
   b. to reduce the amount of radiation emitted by the cloud that reaches the surface and may be reflected there, therefore multiply the downwelling direct radiance $I_0(\tau_{\mathrm{tot}}, \mu)$ in (A6) by $\exp[-\tau_a^{(\mathrm{below})}/|\mu|]$ inside the integral over μ from −1 to 0;
   c. to reduce the amount of radiation indeed reflected by the surface, therefore multiply the surface term in (A3) by the now constant $\exp[-\tau_a^{(\mathrm{below})}/\mu]$;
   d. and to reduce the amount of radiation emitted by the surface and then scattered by the cloud, therefore multiply the upwelling direct surface contribution to $I_0(\tau_z, \mu')$ in (A5) by $\exp[-\tau_a^{(\mathrm{below})}/\mu']$ before the integral over μ' in (A4).
2. $\tau_a^{(\mathrm{above})}$ is simply used to compute a multiplicative factor, $\exp[-\tau_a^{(\mathrm{above})}/\mu]$, that is applied to the overall result, updated as needed using the above directives for $\tau_a^{(\mathrm{below})} > 0$.

Acknowledgments
This work was partially conducted at the Laboratoire d'Optique Atmosphérique (LOA, UMR 8518, Lille 1 University France) and at the Climate and Radiation Laboratory (NASA/GSFC, code 613) under the NASA Post doctoral Program (NPP) and the Universities Space Research Association (USRA). This research was also carried out partially at the Jet Propulsion Laboratory, California Institute of Technology, under a contract with the National Aeronautics and Space Administration. Furthermore, A.D. acknowledges funding from the Remote Sensing Theory program managed at NASA/HQs by Lucia Tsaoussi. We also thank our anonymous reviewers for their many pertinent comments, leading to much improved quality of the present paper.

References

Aides, A., Y. Y. Schechner, V. Holodovsky, M. J. Garay, and A. B. Davis (2013), Multi sky-view 3D aerosol distribution recovery, *Opt. Express*, *21*(22), 25,820–25,833, doi:10.1364/OE.21.025820.

Anderson, G. P. (1986), AFGL atmospheric constituent profiles (0–120 km), *AFGL-TR 86-0110*, Hanscom AFB Mass., U.S.

Baran, A. J. (2012), From the single-scattering properties of ice crystals to climate prediction: A way forward, *Atmos. Res.*, *112*, 45–69.

Baran, A. J., and P. N. Francis (2004), On the radiative properties of cirrus cloud at solar and thermal wavelengths: A test of model consistency using high-resolution airborne radiance measurements, *Q. J. R. Meteorol. Soc.*, *130*(598), 763–778, doi:10.1256/qj.03.151.

Baran, A. J., P. J. Connolly, and C. Lee (2009), Testing an ensemble model of cirrus ice crystals using midlatitude in situ estimates of ice water content, volume extinction coefficient and the total solar optical depth, *J. Quant. Spectrosc. Radiat. Transfer*, *110*(14–16), 1579–1598.

Baran, A. J., R. Cotton, K. Furtado, S. Havemann, L.-C. Labonnote, F. Marenco, A. Smith, and J.-C. Thelen (2013), A self-consistent scattering model for cirrus. II: The high and low frequencies, *Q. J. R. Meteorol. Soc.*, *140*, 1039–1057.

Baum, B., A. Heymsfield, P. Yang, S. Platnick, M. King, Y.-X. Hu, and S. Bedka (2005a), Bulk scattering models for the remote sensing of ice clouds. Part I: Microphysical data and models, *J. Appl. Meteorol.*, *44*(12), 1885–1895.

Baum, B., P. Yang, A. Heymsfield, S. Platnick, M. King, Y.-X. Hu, and S. Bedka (2005b), Bulk scattering properties for the remote sensing of ice clouds. Part II: Narrowband models, *J. Appl. Meteorol.*, *44*(12), 1896–1911.

Benassi, A., F. Szczap, A. Davis, M. Masbou, C. Cornet, and P. Bleuyard (2004), Thermal radiative fluxes through inhomogeneous cloud fields: A sensitivity study using a new stochastic cloud generator, *Atmos. Res.*, *72*, 291–315.

Cahalan, R. F., and J. B. Snider (1989), Marine stratocumulus structure, *Remote Sens. Environ.*, *28*, 95–107.

Cahalan, R. F., W. Ridgway, W. J. Wiscombe, T. L. Bell, and J. B. Snider (1994), The albedo of fractal stratocumulus clouds, *J. Atmos. Sci.*, *51*(16), 2434–2455.

Chen, Y., and K. N. Liou (2006), A Monte Carlo method for 3D thermal infrared radiative transfer, *J. Quant. Spectrosc. Radiat. Transfer*, *101*, 166–178.

Chepfer, H., J. Pelon, G. Brogniez, C. Flamant, V. Trouillet, and P. H. Flamant (1999), Impact of cirrus cloud ice crystal shape and size on multiple scattering effects: Application to spaceborne and airborne backscatter lidar measurements during LITE mission and E-LITE campaign, *Geophys. Res. Lett.*, *26*(14), 2203–2206, doi:10.1029/1999GL900474.

Cooper, S. J., T. S. L'Ecuyer, P. Gabriel, A. J. Baran, and G. L. Stephens (2007), Performance assessment of a five-channel estimation-based ice cloud retrieval scheme for use over the global oceans, *J. Geophys. Res.*, *112*, D04207, doi:10.1029/2006JD007122.

Cornet, C., L.-C. Labonnote, and F. Szczap (2010), Three-dimensional polarized Monte Carlo atmospheric radiative transfer model (3DMCPOL): 3D effects on polarized visible reflectances of a cirrus cloud, *J. Quant. Spectrosc. Radiat. Transfer*, *111*(1), 174–186.

Corti, T., and T. Peter (2009), A simple model for cloud radiative forcing, *Atmospheric . Chem. Phys.*, *9*, 5751–5758.

Davis, A., A. Marshak, W. Wiscombe, and R. Cahalan (1994), Multifractal characterizations of nonstationarity and intermittency in geophysical fields: Observed, retrieved, or simulated, *J. Geophys. Res.*, *99*(D4), 8055–8072.

Davis, A., A. Marshak, W. Wiscombe, and R. Cahalan (1996), Scale invariance of liquid water distributions in marine stratocumulus. Part I: Spectral properties and stationarity issues, *J. Atmos. Sci.*, *53*, 1538–1558.

Davis, A., A. Marshak, R. Cahalan, and W. Wiscombe (1997), The Landsat scale break in stratocumulus as a three-dimensional radiative transfer effect: Implications for cloud remote sensing, *J. Atmos. Sci.*, *54*, 241–260, doi:10.1175/1520-0469(1997)054<0241:TLSBIS>2.0.CO;2.

Davis, A. B., A. Marshak, H. Gerber, and W. J. Wiscombe (1999), Horizontal structure of marine boundary layer clouds from centimeter to kilometer scales., *J. Geophys. Res.*, *104*(D6), 6123–6144.

Emde, C., R. Buras, and B. Mayer (2011), ALIS: An efficient method to compute high spectral resolution polarized solar radiances using the Monte Carlo approach, *J. Quant. Spectrosc. Radiat. Transfer*, *112*, 1622–1631.

Fauchez, T., C. Cornet, F. Szczap, and P. Dubuisson (2012), *Assessment of Cloud Heterogeneities Effects on Brightness Temperatures Simulated With a 3D Monte Carlo Code in the Thermal Infrared*, paper presented at International Radiation Symposium, p. 4, Berlin, Germany.

Fauchez, T., C. Cornet, F. Szczap, P. Dubuisson, and T. Rosambert (2014), Impacts of cirrus clouds heterogeneities on top-of-atmosphere thermal infrared radiation, *Atmos. Chem. Phys.*, *14*, 5599–5615, doi:10.5194/acp-14-5599-2014.

Fauchez, T., P. Dubuisson, C. Cornet, F. Szczap, A. Garnier, J. Pelon, and K. Meyer (2015), Impacts of cloud heterogeneities on cirrus optical properties retrieved from space-based thermal infrared radiometry, *Atmos. Meas. Tech.*, *8*(2), 633–647, doi:10.5194/amt-8-633-2015.

Field, P., A. Heymsfield, and A. Bansemer (2007), Snow size distribution parameterization for midlatitude and tropical ice clouds, *J. Atmos. Sci.*, *64*, 4346–4365.

Field, P. R., R. J. Hogan, P. R. A. Brown, A. J. Illingworth, T. W. Choularton, and R. J. Cotton (2005), Parametrization of ice-particle size distributions for mid-latitude stratiform cloud, *Q. J. R. Meteorol. Soc.*, *131*(609), 1997–2017.

Gabriel, P. M., and K. F. Evans (1996), Simple radiative transfer methods for calculating domain-averaged solar fluxes in inhomogeneous clouds, *J. Atmos. Sci.*, *53*(6), 858–877, doi:10.1175/1520-0469(1996)053<0858:SRTMFC>2.0.CO;2.

Garnier, A., J. Pelon, P. Dubuisson, M. Faivre, O. Chomette, N. Pascal, and D. P. Kratz (2012), Retrieval of cloud properties using CALIPSO imaging infrared radiometer. Part I: Effective emissivity and optical depth, *J. Appl. Meteorol. Climatol.*, *51*, 1407–1425.

Garnier, A., J. Pelon, P. Dubuisson, P. Yang, M. Faivre, O. Chomette, N. Pascal, P. Lucker, and T. Murray (2013), Retrieval of cloud properties using CALIPSO imaging infrared radiometer. Part II: Effective diameter and ice water path, *J. Appl. Meteorol. Climatol.*, *52*, 2582–2599.

Garnier, A., J. Pelon, M. A. Vaughan, D. M. Winker, C. Trepte, and P. Dubuisson (2015), Lidar multiple scattering factors inferred from CALIPSO lidar and IIR retrievals of semi-transparent cirrus cloud optical depths over oceans, *Atmos. Meas. Tech.*, *8*(7), 2759–2774, doi:10.5194/amt-8-2759-2015.

Gerber, H., J. B. Jensen, A. B. Davis, A. Marshak, and W. J. Wiscombe (2001), Spectral density of cloud liquid water content at high frequencies, *J. Atmos. Sci.*, *58*(5), 497–503.

Harshvardhan, and J. A. Weinman (1982), Infrared radiative transfer through a regular array of cuboidal clouds, *J. Atmos. Sci.*, *39*(2), 431–439, doi:10.1175/1520-0469(1982)039<0431:IRTTAR>2.0.CO;2.

Heidinger, A. K., and S. K. Cox (1996), Finite-cloud effects in longwave radiative transfer, *J. Atmos. Sci.*, *53*(7), 953–963, doi:10.1175/1520-0469(1996)053<0953:FCEILR>2.0.CO;2.

Hogan, R. J., and S. F. Kew (2005), A 3D stochastic cloud model for investigating the radiative properties of inhomogeneous cirrus clouds, *Q. J. R. Meteorol. Soc.*, *131*(611), 2585–2608.

Holz, R. E., et al. (2016), Resolving ice cloud optical thickness biases between CALIOP and MODIS using infrared retrievals, *Atmos. Chem. Phys.*, *16*(8), 5075–5090, doi:10.5194/acp-16-5075-2016.

Inoue, T. (1985), On the temperature and effective emissivity determination of semi-transparent cirrus clouds by bi-spectral measurements in the 10 µm window region, *J. Meteorol. Soc. Jpn.*, *63*, 88–99.

Jensen, E. J., S. Kinne, and O. B. Toon (1994), Tropical cirrus cloud radiative forcing: Sensitivity studies, *Geophys. Res. Lett.*, *21*, 2023–2026, doi:10.1029/94GL01358.

Kahn, B. H., et al. (2014), The Atmospheric Infrared Sounder version 6 cloud products, *Atmos. Chem. Phys.*, *14*(1), 399–426, doi:10.5194/acp-14-399-2014.

Kahn, B. H., M. M. Schreier, Q. Yue, E. J. Fetzer, F. W. Irion, S. Platnick, C. Wang, S. L. Nasiri, and T. S. L'Ecuyer (2015), Pixel-scale assessment and uncertainty analysis of AIRS and MODIS ice cloud optical thickness and effective radius, *J. Geophys. Res. Atmos.*, *120*, 11,669–11,689, doi:10.1002/2015JD023950.

Katagiri, S., T. Hayasaka, A. Shimizu, I. Matsui, T. Nishizawa, N. Sugimoto, and T. Takamura (2013), Long term analysis of cirrus clouds: Effects on shortwave and longwave radiation derived from data acquired by ground-based and satellite-borne observations, *AIP Conf. Proc.*, *1531*(1), 492–495, doi:10.1063/1.4804814.

Kew, S. (2003), Development of a 3D fractal cirrus model and its use in investigating the impact of cirrus inhomogeneity on radiation, Master's thesis, Dept. of Math., Univ. of Reading, Reading, U. K.

Kratz, D. P. (1995), The correlated k-distribution technique as applied to the AVHRR channels, *J. Quant. Spectrosc. Radiat. Transfer*, *53*, 501–517.

Lacis, A. A., and V. Oinas (1991), A description of the correlated-k distribution method for modeling nongray gaseous absorption, thermal emission, and multiple scattering in vertically inhomogeneous atmospheres, *J. Geophys. Res.*, *96*(D5), 9027–9063.

Liou, K.-N., and S.-C. Ou (1979), Infrared radiative transfer in finite cloud layers, *J. Atmos. Sci.*, *36*(10), 1985–1996, doi:10.1175/1520-0469(1979)036<1985:IRTIFC>2.0.CO;2.

Marshak, A., and A. B. Davis (2005), *3D Radiative Transfer in Cloudy Atmospheres, Phys. of Earth and Space Environ. Ser.*, Springer, Heidelberg, Germany.

Mayer, B. (2009), Radiative transfer in the cloudy atmosphere, *Eur. Phys. J. Conf.*, *1*, 75–99.

Min, M., P. Wang, J. R. Campbell, X. Zong, and Y. Li (2010), Midlatitude cirrus cloud radiative forcing over China, *J. Geophys. Res.*, *115*, D20210, doi:10.1029/2010JD014161.

Nakajima, T., and M. D. King (1990), Determination of the optical thickness and effective particle radius of clouds from reflected solar radiation measurements. Part I: Theory, *J. Atmos. Sci.*, *47*(15), 1878–1893.
Oreopoulos, L., and R. F. Cahalan (2005), Cloud inhomogeneity from MODIS, *J. Clim.*, *18*, 5110–5124.
Parol, F., J.-C. Buriez, G. Brogniez, and Y. Fouquart (1991), Information content of AVHRR channels 4 and 5 with respect to the effective radius of cirrus cloud particles, *J. Appl. Meteorol.*, *30*, 973–984.
Partain, P. T., A. K. Heidinger, and G. L. Stephens (2000), High spectral resolution atmospheric radiative transfer: Application of the equivalence theorem, *J. Geophys. Res.*, *105*, 2163–2177.
Platnick, S., M. D. King, S. A. Ackerman, W. P. Menzel, B. A. Baum, J. C. Riedi, and R. A. Frey (2003), The MODIS cloud products: Algorithms and examples from Terra, *IEEE Trans. Geosci. Remote Sens.*, *41*, 459–473.
Platnick, S., et al. (2015), MODIS cloud optical properties: User guide for the Collection 6 level-2 MOD06/MYD06 product and associated level-3 dataset, Tech. Rep., GSFC MODIS TEAM, Goddard Space Flight Center.
Pujol, O. (2015), Comment on the (misused) concept of photon in radiative transfer, and proposition of a neologism, *J. Quant. Spectrosc. Radiat. Transfer*, *159*, 29–31, doi:10.1016/j.jqsrt.2015.02.024.
Reichardt, J., M. Hess, and A. Macke (2000), Lidar inelastic multiple-scattering parameters of cirrus particle ensembles determined with geometrical-optics crystal phase functions, *Appl. Opt.*, *39*(12), 1895–1910.
Rodgers, C. D. (2000), *Inverse Methods for Atmospheric Sounding Theory and Practice*, World Sci., Tokyo.
Sassen, K., Z. Wang, and D. Liu (2008), Global distribution of cirrus clouds from CloudSat/Cloud-Aerosol Lidar and Infrared Pathfinder Satellite Observations (CALIPSO) measurements, *J. Geophys. Res.*, *113*, D00A12, doi:10.1029/2008JD009972.
Sourdeval, O., L. C. Labonnote, A. J. Baran, and G. Brogniez (2015), A methodology for simultaneous retrieval of ice and liquid water cloud properties. Part I: Information content and case study, *Q. J. R. Meteorol. Soc.*, *141*(688), 870–882, doi:10.1002/qj.2405.
Szczap, F., H. Isaka, M. Saute, B. Guillemet, and Y. Gour (2000), Inhomogeneity effects of 1D and 2D bounded cascade model clouds on their effective radiative properties, *Phys. Chem. Earth Part B*, *25*(2), 83–89.
Szczap, F., Y. Gour, T. Fauchez, C. Cornet, T. Faure, O. Jourdan, and P. Dubuisson (2014), 3DCLOUD, a fast and flexible 3D cloud optical depth generator based on drastically simplified basic atmospheric equations and Fourier transform framework: Applications to stratocumulus, cumulus and cirrus cloud fields, *Geosci. Model Dev.*, *7*(1), 1779–1801.
Twomey, S. A., C. F. Bohren, and J. L. Mergenthaler (1986), Reflectance and albedo differences between wet and dry surfaces, *Appl. Opt.*, *25*(3), 431–437, doi:10.1364/AO.25.000431.
van de Hulst, H. C. (1974), The spherical albedo of a planet covered with a homogeneous cloud layer, *Astrophys. J.*, *35*, 209–214.
Várnai, T., and R. Davies (1999), Effects of cloud heterogeneities on shortwave radiation: Comparison of cloud-top variability and internal heterogeneity, *J. Atmos. Sci.*, *56*, 4206–4224.
Várnai, T., and A. Marshak (2001), Statistical analysis of the uncertainties in cloud optical depth retrievals caused by three-dimensional radiative effects, *J. Atmos. Sci.*, *58*(12), 1540–1548.
Wang, C., S. E. Platnick, K. Meyer, and Z. Zhang (2014), Infrared retrievals of ice cloud properties and uncertainties with an optimal estimation retrieval method, Abstract A23P-06 presented at 2014 Fall Meeting AGU.
Wang, C., S. Platnick, Z. Zhang, K. Meyer, and P. Yang (2016a), Retrieval of ice cloud properties using an optimal estimation algorithm and MODIS infrared observations. Part I: Forward model, error analysis, and information content, *J. Geophys. Res. Atmos.*, *121*, 5809–5826, doi:10.1002/2015JD024526.
Wang, C., S. Platnick, Z. Zhang, K. Meyer, G. Wind, and P. Yang (2016b), Retrieval of ice cloud properties using an optimal estimation algorithm and MODIS infrared observations. Part II: Retrieval evaluation, *J. Geophys. Res. Atmos.*, *121*, 5827–5845, doi:10.1002/2015JD024528.
Wang, L., and K. Sassen (2008), Wavelet analysis of cirrus multiscale structures from lidar backscattering: A cirrus uncinus complex case study, *J. Appl. Meteorol. Climatol.*, *47*(10), 2645–2658, doi:10.1175/2008JAMC1788.1.
Wang, X., A. Boselli, L. D'Avino, R. Velotta, N. Spinelli, P. Bruscaglioni, A. Ismaelli, and G. Zaccanti (2005), An algorithm to determine cirrus properties from analysis of multiple-scattering influence on lidar signals, *Appl. Phys. B*, *80*(4–5), 609–615, doi:10.1007/s00340-005-1765-x.
Yang, P., B.-C. Gao, B. A. Baum, Y. X. Hu, W. J. Wiscombe, S.-C. Tsay, D. M. Winker, and S. L. Nasiri (2001), Radiative properties of cirrus clouds in the infrared (8–13 μm) spectral region, *J. Quant. Spectrosc. Radiat. Transfer*, *70*(4-6), 473–504.
Yang, P., H. Wei, H.-L. Huang, B. A. Baum, Y. X. Hu, G. W. Kattawar, M. I. Mishchenko, and Q. Fu (2005), Scattering and absorption property database for nonspherical ice particles in the near- through far-infrared spectral region, *Appl. Opt.*, *44*(26), 5512–5523.